Ultrasonics Sonochemistry 97 (2023) 106455

Contents lists available at ScienceDirect

Ultrasonics Sonochemistry

journal homepage: www.elsevier.com/locate/ultson

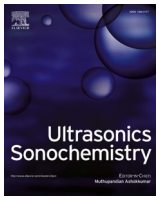

Weakly nonlinear focused ultrasound in viscoelastic media containing multiple bubbles

Shunsuke Kagami [a], Tetsuya Kanagawa [b,*]

[a] Department of Engineering Mechanics and Energy, Degree Programs in Systems and Information Engineering, University of Tsukuba, 1-1-1 Tennodai, Tsukuba 305-8573, Japan
[b] Department of Engineering Mechanics and Energy, Institute of Systems and Information Engineering, University of Tsukuba, 1-1-1 Tennodai, Tsukuba 305-8573, Japan

ARTICLE INFO

Keywords:
Focused ultrasound
Viscoelastic media
Bubbly liquid
Weakly nonlinear wave
KZK equation
HIFU

ABSTRACT

To facilitate practical medical applications such as cancer treatment utilizing focused ultrasound and bubbles, a mathematical model that can describe the soft viscoelasticity of human body, the nonlinear propagation of focused ultrasound, and the nonlinear oscillations of multiple bubbles is theoretically derived and numerically solved. The Zener viscoelastic model and Keller–Miksis bubble equation, which have been used for analyses of single or few bubbles in viscoelastic liquid, are used to model the liquid containing multiple bubbles. From the theoretical analysis based on the perturbation expansion with the multiple-scales method, the Khokhlov–Zabolotskaya–Kuznetsov (KZK) equation, which has been used as a mathematical model of weakly nonlinear propagation in single phase liquid, is extended to viscoelastic liquid containing multiple bubbles. The results show that liquid elasticity decreases the magnitudes of the nonlinearity, dissipation, and dispersion of ultrasound and increases the phase velocity of the ultrasound and linear natural frequency of the bubble oscillation. From the numerical calculation of resultant KZK equation, the spatial distribution of the liquid pressure fluctuation for the focused ultrasound is obtained for cases in which the liquid is water or liver tissue. In addition, frequency analysis is carried out using the fast Fourier transform, and the generation of higher harmonic components is compared for water and liver tissue. The elasticity suppresses the generation of higher harmonic components and promotes the remnant of the fundamental frequency components. This indicates that the elasticity of liquid suppresses shock wave formation in practical applications.

1. Introduction

The combination of ultrasound and bubbles has been utilized in a wide range of medical applications, for both treatment and diagnosis [1]. In tumor ablation therapy, the thermal effects radiated by oscillating bubbles improve the heating effect of high-intensity focused ultrasound (HIFU) [2–10]. Shock wave lithotripsy and histotripsy therapies use the oscillation or collapse of cavitation bubbles induced by the mechanical effects of HIFU to eradicate kidney stones and cancer cells [11–20]. Ultrasound also induces the oscillation or collapse of bubbles injected into blood vessels during drug delivery to brain cancer cells, which opens the blood–brain barrier [21]. Moreover, bubbles encapsulated by lipid shells improve the resolution of images [22–31] for ultrasound imaging as a real-time diagnostic technique.

For these medical applications, the investigation of bubble dynamics in soft viscoelastic media like human body is essential. Newtonian fluid is the most famous model in the field of fluid dynamics, but only viscosity is considered. The Kelvin–Voigt [19,30–39] and Zener models [41–47] have been used as mathematical models of liquid with viscoelasticity. The Kelvin–Voigt model corresponds to the generalized Newtonian fluid with the elasticity introduced while the relaxation effect is omitted. Yang and Church [34] investigated a behavior of single spherical bubble based on the Kelvin–Voigt model and Keller–Miksis equation [19,34–44,52], and showed that liquid elasticity decreases the nonlinearity of bubble oscillation. Keller–Miksis equation is a model of bubble dynamics in compressible and viscoelastic liquid and often used in combination with Kelvin–Voigt model [34–36,38–40]. Murakami et al. [37] developed a model of the behavior of a non-spherical single bubble based on the Kelvin–Voigt model and Rayleigh–Plesset equation and investigated the shape stability of bubbles. Rayleigh–Plesset equation is the most famous model of bubble dynamics, but is the limiting case of Keller–Miksis equation assuming the incompressible liquid. Qin

* Corresponding author.
E-mail address: kanagawa.tetsuya.fu@u.tsukuba.ac.jp (T. Kanagawa).

https://doi.org/10.1016/j.ultsonch.2023.106455
Received 19 February 2023; Received in revised form 12 May 2023; Accepted 23 May 2023
Available online 27 May 2023

et al. [39] investigated the effects of the liquid viscoelasticity and the interaction of two bubbles on behavior of each bubble using the Kelvin–Voigt model and Keller–Miksis equation. The Maxwell viscoelastic model [48–51] is also the generalized Newtonian fluid with the relaxation effect of viscoelastic medium, however the elastic term is omitted. Fogler and Goddard [48] investigated the collapse of bubble in viscoelastic media based on the Maxwell model and Rayleigh–Plesset equation.

Further, the Zener model corresponds to the generalized Kelvin–Voigt and Maxwell model, including the elastic term and the relaxation effect of a viscoelastic medium. Warnez and Johnsen [42] developed a numerical method for bubble behavior based on the Zener model and Keller–Miksis equation, and they found that incorporating the relaxation time increases bubble growth. Zilonova et al. [46] investigated the interaction of two bubbles with the effects of drag force and translation based on the Zener model and Gilmore–Akulichev equation [53]. Gilmore–Akulichev equation has broader applications than the Keller–Miksis equation [46,47]. Filonets and Solovchuk [47] investigated the single bubble behavior excited by a dual-frequency ultrasound based on the Zener model and Gilmore–Akulichev equation, and they showed that the elasticity of a liquid increases the threshold pressure of bubble collapse.

Therefore, the behavior of a single or few bubbles in viscoelastic liquid has been well investigated; however, considering multiple bubbles from a macroscopic view is necessary for practical medical applications. The Westervelt equation [54] for full-wave propagation and the Khokhlov–Zabolotskaya–Kuznetsov (KZK) equation [55,56] for quasi-planar propagation have both been used as continuum models for the nonlinear propagation of focused ultrasound. The KZK equation corresponds to the limiting form of the Westervelt equation and has been widely used [57–87] as a computational model for medical applications, owing to its accuracy and usability in numerical calculations. However, the original KZK equation [55,56] was derived for propagation in single phase liquids without bubbles.

The authors were involved in the first derivation of the KZK equation for a liquid containing multiple bubbles [88–90], using theoretical analysis based on volumetric averaged basic equations for liquids containing multiple bubbles. Kagami and Kanagawa [10] introduced the thermal effects of gas inside the bubbles into the KZK equation and obtained numerical solutions. However, these models [10,88–90] only considered viscosity and neglected the elasticity of the liquid. Recently, Hasegawa et al. [91] succeeded in introducing the elasticity of a liquid into the weakly nonlinear wave equation; however, this model was limited to the spatial one-dimensional form and could not be used for focused ultrasound. In addition, the viscoelasticity of the bubble–liquid interface was considered, but not the viscoelasticity of the entire liquid. In summary, a mathematical model that can describe the liquid viscoelasticity of both the bubble–liquid interface and the entire liquid, the nonlinear propagation of focused ultrasound, and the oscillations of multiple bubbles would be very useful.

In this study, the KZK equation describing the weakly nonlinear propagation of focused ultrasound in a viscoelastic liquid containing multiple bubbles is derived. In Section 2, volumetric averaged equations for a liquid containing multiple bubbles are introduced, based on the mixture model [96–99]. The viscoelasticities of the entire liquid and bubble–liquid interface are introduced, as shown in Fig. 1. The momentum conservation equation in the mixture model is combined with the Zener model to incorporate the viscoelasticity of the entire liquid, and the Keller–Miksis equation for bubble dynamics is used to incorporate the viscoelasticity of the bubble–liquid interface. Theoretical analysis based on the perturbation expansion and multiple-scales method [121] is carried out in Section 3, and the derivation of the KZK equation is demonstrated. This KZK equation is composed of terms representing the nonlinear, dissipation, dispersion, and diffraction effects of ultrasound propagation. The effects of the liquid elasticities on the nonlinearity, dissipation, dispersion, and phase velocity of focused ultrasound and the natural frequency of bubble oscillation are investigated by comparing cases in which the liquid is water (without elasticities) or liver tissue (with elasticities). By a comparison among the Zener model, the Maxwell model, and the Kelvin–Voigt model, the effects of the rigidity and the relaxation time are compared. In addition, a comparison of the liquid viscoelasticity of the entire liquid and bubble–liquid interface is conducted. In Section 4, the numerical solution of the newly obtained KZK equation is presented. The spatial distribution of the fluctuation of liquid pressure for the focused ultrasound is obtained. The dispersion effect on the numerical solution appeared. In addition, frequency analysis is conducted using the fast Fourier transform (FFT), and the generation of higher harmonic components is compared for water and liver tissue. As a result, the elasticity of liver tissue suppresses the generation of higher harmonic components and promotes the remnant of the fundamental frequency components compare to the case of water, although the maximum value of the rise of liquid pressure are quite close. This result implies that the elasticity of liquid suppresses shock wave formation in practical applications.

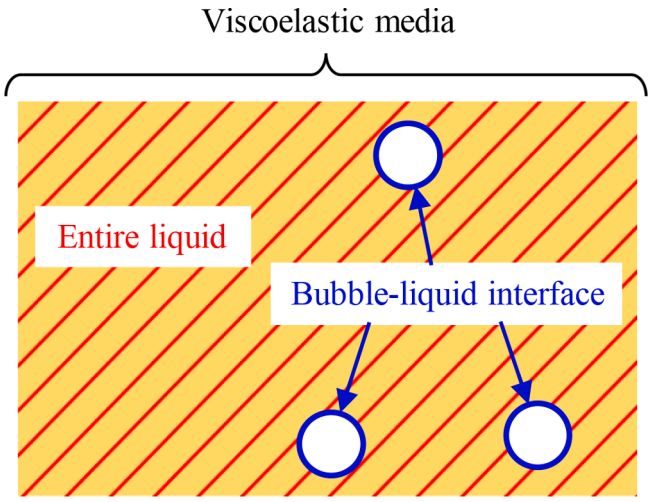

Fig. 1. Regions in which viscoelasticity is considered.

2. Formulation of the problem

2.1. Problem statement

The weakly nonlinear propagation of focused ultrasound in a liquid containing multiple bubbles is considered. In this study, the viscoelasticity of the liquid phase is considered in two regions: the entire liquid and the bubble–liquid interface (see Fig. 1).

Focused ultrasound is radiated from a sound source in a viscoelastic medium containing multiple bubbles (Fig. 2). The center of the sound

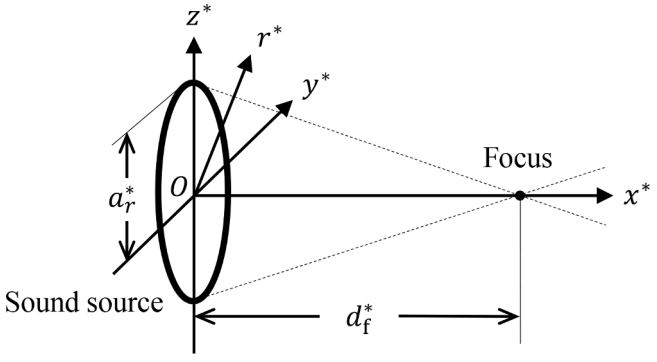

Fig. 2. Schematic of spatial coordinates. Ultrasound radiated from a circular sound source with focused beam.

source is set as the origin. The x^*-axis represents the distance from sound source, and the r^*-, y^*-, and z^*-axes denote the distances from the x^*-axis. The following relation is provided:

$$r^* = \sqrt{y^{*2} + z^{*2}}. \tag{1}$$

Note that the surface shape of the sound source is not only focusing, but can also be in a planar or spreading form, and the shape profile of the sound source is not only circular, but can also be rectangular or elliptical.

The KZK equation is derived by assuming quasi-plane propagation, i.e., weakly diffracted (focused or spreading) waves. In this study, two types of KZK equations are derived: two-dimensional (2D) and three-dimensional (3D) spatial forms, as in our previous work [10]. Although the 2D KZK equation is assumed for axial symmetric ultrasound, the 3D KZK equation can handle asymmetric propagation, such as ultrasound radiated by an elliptical or rectangular sound source or propagated in a nonuniform medium, such as the human body. The following relation is provided as a mathematical formula of the quasi-plane waves [10,88,90,93]:

$$R_0^* \ll L^* \ll a_i^*, \tag{2}$$

where R_0^* is the initial bubble radius, L^* is the typical ultrasound wavelength, and a_i^* $(i = r,y,z)$ are typical lengths in each direction; a_r^* is set as the radius of circular sound source, and a_y^* and a_z^* are set as the long and short diameters of elliptic sound sources, or the width and height of rectangular sound sources, etc.

In the theoretical analysis, the following assumptions are introduced for simplicity.

(a-1) The elasticity of the liquid phase is considered; however, the viscoelastic shells [23,25–31] coating the bubbles are not.
(a-2) The viscosity and elasticity of the gas phase are neglected because they are significantly smaller than those of the liquid phase.
(a-3) The basic equations based on the mixture model [96–99] of bubbly liquids are used; [88,93,94,95] those based on the two-fluid model [99,100] were used in our previous work [10,88–90] because the two-fluid model needs many assumptions and experimental laws to incorporate the viscoelasticity of the liquid phase. Note that the mixture model requires some assumptions such as (a-4) and (a-6) described below.
(a-4) The difference of velocity between the gas and liquid phases is sufficiently small, and then the drag force [102,103] is not considered.
(a-5) The initial void fraction is sufficiently small.
(a-6) The viscosity and elasticity of the gas–liquid mixture are modeled by only those of the liquid phase, because the viscosity and elasticity of the gas phase are sufficiently smaller than those of the liquid phase according to assumptions (a-2) and (a-5).
(a-7) The bubble–bubble interaction [39,44,46,104–106], which may be dominant under high void fraction, is not considered.
(a-8) Bubble oscillation is spherically symmetric.
(a-9) Bubbles do not collapse, appear, or coalesce.
(a-10) The phase change [107–109] and the heat transfer [110] at the bubble–liquid interface is not considered.
(a-11) The distributions of the pressure and temperature of the gas inside the bubbles [101] are not considered; they are treated as the averages inside each bubble.
(a-12) The temperature of the liquid phase is assumed constant, whereas the temperature of the gas phase is assumed to fluctuate.
(a-13) At initial state, the liquid is at rest and spatially uniform, except for the spatial distribution of bubbles. The nonuniformity of the bubble size [111–115] is not considered. The spatial nonuniformity of the bubble distribution at the initial state is introduced [88,90,93] because bubbles are only used in focus in medical applications.

2.2. Basic equations

The conservation laws of mass and momentum based on the mixture model [96–99] are used:

$$\frac{\partial \rho^*}{\partial t^*} + \nabla^* \cdot (\rho^* \boldsymbol{u}^*) = 0, \tag{3}$$

$$\frac{\partial \rho^* \boldsymbol{u}^*}{\partial t^*} + \nabla^* \cdot (\rho^* \boldsymbol{u}^* \boldsymbol{u}^*) + \nabla^* p_{\mathrm{L}}^* - \lambda_{\mathrm{v,L}}^* \nabla^* (\nabla^* \cdot \boldsymbol{u}^*) - \lambda_{\mathrm{e,L}}^* \nabla^* (\nabla^* \cdot \boldsymbol{d}^*) - \nabla^* \cdot \boldsymbol{\tau}^* = \boldsymbol{0}, \tag{4}$$

where t^* is time, ρ^* is density, $\boldsymbol{u}^*$ is the velocity vector, $\boldsymbol{d}^*$ is the displacement vector, p^* is pressure, $\lambda_{\mathrm{v,L}}^*$ is the second viscosity constant, $\lambda_{\mathrm{e,L}}^*$ is the Lamé constant, and $\boldsymbol{\tau}^*$ is the deviatoric stress tensor. The subscripts G and L mean the values of the gas and liquid phases, respectively. In (4), the pressure of the mixture is assumed to be that of the liquid phase [89,93,94]. The density of the gas phase is generally sufficiently small; hence, the density of the mixture is defined by the liquid density as follows:

$$\rho^* \equiv (1-\alpha)\rho_{\mathrm{L}}^*, \tag{5}$$

where α is the void fraction

$$\alpha = \frac{4}{3}\pi R^{*3} n^*, \tag{6}$$

where R^* is the bubble radius, n^* is the bubble number density, and the following conservation law is imposed:

$$\frac{\partial n^*}{\partial t^*} + \nabla^* \cdot (n^* \boldsymbol{u}^*) = 0. \tag{7}$$

The conservation of mass in each bubble is

$$\frac{\rho_{\mathrm{G}}^*}{\rho_{\mathrm{G0}}^*} = \left(\frac{R_0^*}{R^*}\right)^3. \tag{8}$$

The second viscosity $\lambda_{\mathrm{v,L}}^*$ and Lamé constant $\lambda_{\mathrm{e,L}}^*$ can be rewritten as follows:

$$\lambda_{\mathrm{v,L}}^* = K_{\mathrm{v,L}}^* - \frac{2}{3}\mu_{\mathrm{L}}^*, \tag{9}$$

$$\lambda_{\mathrm{e,L}}^* = K_{\mathrm{e,L}}^* - \frac{2}{3}G_{\mathrm{L}}^*, \tag{10}$$

where $K_{\mathrm{v,L}}^*$ and $K_{\mathrm{e,L}}^*$ are the bulk viscosity and elasticity, respectively; μ_{L}^* is the viscosity; and G_{L}^* is the rigidity (shear modulus). The bulk viscosity $K_{\mathrm{v,L}}^*$ was set to zero based on the Stokes assumption [93,94]. The physical quantities in (9) and (10) were originally that of the gas–liquid mixture; however, they have been substituted by that of the liquid phase from assumption (a-6) in Section 2.1.

Equations (6) and (8) are substituted into (7), equation (5) into (3) and (4), and (9), (10), and $K_{\mathrm{v,L}}^* = 0$ into (4) to obtain the following equations:

$$\frac{\partial \alpha \rho_{\mathrm{G}}^*}{\partial t^*} + \nabla^* \cdot (\alpha \rho_{\mathrm{G}}^* \boldsymbol{u}^*) = 0, \tag{11}$$

$$\frac{\partial}{\partial t^*}[(1-\alpha)\rho_{\mathrm{L}}^*] + \nabla^* \cdot [(1-\alpha)\rho_{\mathrm{L}}^* \boldsymbol{u}^*] = 0, \tag{12}$$

$$\frac{\partial}{\partial t^*}[(1-\alpha)\rho_{\mathrm{L}}^* \boldsymbol{u}^*] + \nabla^* \cdot [(1-\alpha)\rho_{\mathrm{L}}^* \boldsymbol{u}^* \boldsymbol{u}^*] + \nabla^* p_{\mathrm{L}}^* + \frac{2}{3}\mu_{\mathrm{L}}^* \nabla^* (\nabla^* \cdot \boldsymbol{u}^*) - \left(K_{\mathrm{e,L}}^* - \frac{2}{3}G_{\mathrm{L}}^*\right)\nabla^* (\nabla^* \cdot \boldsymbol{d}^*) - \nabla^* \cdot \boldsymbol{\tau}^* = \boldsymbol{0}. \tag{13}$$

The velocity $\boldsymbol{u}^*$ and displacement $\boldsymbol{d}^*$ can be related as follows:

$$\boldsymbol{u}^* = \frac{\mathrm{D}\boldsymbol{d}^*}{\mathrm{D}t^*}, \tag{14}$$

where the Lagrange derivative $\mathrm{D}/\mathrm{D}t^*$ is the differential operator:

$$\frac{\mathrm{D}}{\mathrm{D}t^*} = \frac{\partial}{\partial t^*} + \boldsymbol{u}^* \cdot \nabla^*. \tag{15}$$

The deviatoric stress tensor $\boldsymbol{\tau}^*$ is based on the Zener viscoelastic model [41–47]:

$$\boldsymbol{\tau}^* + \lambda_{\mathrm{relax,L}}^* \frac{\mathrm{D}\boldsymbol{\tau}^*}{\mathrm{D}t^*} = 2\mu_{\mathrm{L}}^* \frac{\mathrm{D}\boldsymbol{\gamma}^*}{\mathrm{D}t^*} + 2G_{\mathrm{L}}^* \boldsymbol{\gamma}^*, \tag{16}$$

where $\lambda_{\mathrm{relax,L}}^*$ is the relaxation time of the liquid phase, $\mathrm{D}\boldsymbol{\gamma}^*/\mathrm{D}t^*$ is the velocity gradient tensor, and $\boldsymbol{\gamma}^*$ is the deformation gradient tensor. When $\lambda_{\mathrm{relax,L}}^* = 0$, (16) reduces to the Kelvin–Voigt viscoelastic model [19,30–39]. Further, when $\lambda_{\mathrm{relax,L}}^* = 0$ and $G_{\mathrm{L}}^* = 0$, (16) reduces to a model of Newtonian fluid and the theoretical results reduce to those of our previous studies [10,88,90,93–95,102,113–115]. From (13) and (16), the effect of the viscoelasticity of the entire liquid is introduced.

The Keller–Miksis equation [19,34–44,52] describing spherical bubble oscillation in a compressible viscoelastic liquid is used:

$$\left(1 - \frac{1}{c_{\mathrm{L0}}^*}\frac{\mathrm{D}R^*}{\mathrm{D}t^*}\right)R^* \frac{\mathrm{D}^2 R^*}{\mathrm{D}t^{*2}} + \frac{3}{2}\left(1 - \frac{1}{3c_{\mathrm{L0}}^*}\frac{\mathrm{D}R^*}{\mathrm{D}t^*}\right)\left(\frac{\mathrm{D}R^*}{\mathrm{D}t^*}\right)^2 = \frac{1}{\rho_{\mathrm{L0}}^*}\left(1 + \frac{1}{c_{\mathrm{L0}}^*}\frac{\mathrm{D}R^*}{\mathrm{D}t^*}\right)\left(p_{\mathrm{G}}^* - \frac{2\sigma^*}{R^*} + 3q_{\mathrm{L}}^* - p_{\mathrm{L}}^*\right) + \frac{R^*}{\rho_{\mathrm{L0}}^* c_{\mathrm{L0}}^*}\frac{\mathrm{D}}{\mathrm{D}t^*}\left(p_{\mathrm{G}}^* - \frac{2\sigma^*}{R^*} + 3q_{\mathrm{L}}^*\right), \tag{17}$$

where c_{L0}^* is the speed of sound in pure water and σ^* is the surface tension and the subscript 0 represents initial values. Note that the Keller–Miksis equation can be used for cases in which the Mach number is less than one [46,47], and the Gilmore–Akulichev model [46,47] can be used with larger Mach numbers. The variable q_{L}^* is given by

$$q_{\mathrm{L}}^* = \int_{R^*}^{\infty} \frac{\tau_{r^{*\prime} r^{*\prime} \mathrm{L}}^*}{r^{*\prime}}\, \mathrm{d}r^{*\prime}, \tag{18}$$

where $r^{*\prime}$ is the distance from the center of each bubble. Note that $r^{*\prime}$ is based on the spherical coordinate of each bubble and differs from r^*, which is based on the macroscopic coordinate as shown in Fig. 2. The balance of the normal stresses across the bubble–liquid interface is

$$p_{\mathrm{G}}^* - (p_{\mathrm{L}}^* + P^*) = \frac{2\sigma^*}{R^*} - 3q_{\mathrm{L}}^*. \tag{19}$$

To obtain the constitutive equation for q_{L}^*, the Zener model (16) is integrated from the bubble–liquid interface to infinity [38,39,41,42,44,47]:

$$\lambda_{\mathrm{relax,L}}^* \frac{\mathrm{D}q_{\mathrm{L}}^*}{\mathrm{D}t^*} + q_{\mathrm{L}}^* + \lambda_{\mathrm{relax,L}}^* \frac{1}{R^*}\frac{\mathrm{D}R^*}{\mathrm{D}t^*}\tau_{r^\prime r^\prime \mathrm{L}}^*\big|_{r^\prime = R^*} = \frac{1}{3}\left\{-\frac{4}{3}G_{\mathrm{L}}^*\left[1 - \left(\frac{R_0^*}{R^*}\right)^3\right] - 4\mu_{\mathrm{L}}^* \frac{1}{R^*}\frac{\mathrm{D}R^*}{\mathrm{D}t^*}\right\}. \tag{20}$$

From (17)–(20), the effect of liquid viscoelasticity at the bubble–liquid interface is introduced.

The energy equation describing the thermal conduction at the bubble–liquid interface [116] is used [10,93–95]:

$$\frac{\mathrm{D}p_{\mathrm{G}}^*}{\mathrm{D}t^*} = \frac{3}{R^*}\left[(\kappa - 1)\lambda_{\mathrm{G}}^* \frac{\partial T_{\mathrm{G}}^*}{\partial r^{*\prime}}\bigg|_{r^{*\prime} = R^*} - \kappa p_{\mathrm{G}}^* \frac{\mathrm{D}R^*}{\mathrm{D}t^*}\right], \tag{21}$$

where κ is the ratio of the specific heats of the gas phase, λ^* is the thermal conductivity of the gas phase, and T^* is the temperature. The temperature gradient $\partial T_{\mathrm{G}}^*/\partial r^{*\prime}|_{R^*}$ is substituted into the following model [117]:

$$\frac{\partial T_{\mathrm{G}}^*}{\partial r^{*\prime}}\bigg|_{r^{*\prime} = R^*} = \frac{5}{4}\frac{T_0^* - T_{\mathrm{G}}^*}{R^*}. \tag{22}$$

Note that many temperature gradient models have been proposed, such as Refs. [117–120]; however, the model in (22) [117] derived the most appropriate numerical solution of the models in our previous work [10] and is used again in this study. To close the set of equations, the Tait equation of state for the liquid phase and the equation of state for an ideal gas are used:

$$p_{\mathrm{L}}^* = p_{\mathrm{L0}}^* + \frac{\rho_{\mathrm{L0}}^* c_{\mathrm{L0}}^{*2}}{n}\left[\left(\frac{\rho_{\mathrm{L}}^*}{\rho_{\mathrm{L0}}^*}\right)^n - 1\right], \tag{23}$$

$$\frac{p_{\mathrm{G}}^*}{p_{\mathrm{G0}}^*} = \frac{\rho_{\mathrm{G}}^*}{\rho_{\mathrm{G0}}^*}\frac{T_{\mathrm{G}}^*}{T_0^*}, \tag{24}$$

where n is the material constant (e.g., $n = 7.15$ for water).

2.3. Parameter scaling

The following scale parameters are introduced to consider the low frequency and long wave as in our previous studies [10,88,89,92–94], using the dimensionless amplitude $\varepsilon (\ll 1)$:

$$\frac{\omega^*}{\omega_{\mathrm{B}}^*} \equiv O(\sqrt{\varepsilon}) \equiv \Omega\sqrt{\varepsilon}, \tag{25}$$

$$\frac{R_0^*}{L^*} \equiv O(\sqrt{\varepsilon}) \equiv \Delta\sqrt{\varepsilon}, \tag{26}$$

$$\frac{U^*}{c_{\mathrm{L0}}^*} \equiv O(\sqrt{\varepsilon}) \equiv V\sqrt{\varepsilon}, \tag{27}$$

where ω^*, L^*, and U^* are the typical angular frequency, wavelength, and propagation speed, respectively, and Ω, Δ, and V are the dimensionless constants of $O(1)$.

The assumption of weakly diffracted waves given by (2) is rewritten as follows ($i = r, y, z$) [10]:

$$\frac{L^*}{a_i^*} \equiv O(\sqrt{\varepsilon}) \equiv \Gamma_i\sqrt{\varepsilon}, \tag{28}$$

where the dimensionless constant Γ_i of $O(1)$ represents the degree of diffraction for each direction.

The liquid viscosity μ_{L}^*, rigidity G_{L}^*, bulk elasticity $K_{\mathrm{e,L}}^*$, and relaxation time $\lambda_{\mathrm{relax,L}}^*$ are nondimensionalized as

$$\frac{\mu_{\mathrm{L}}^*}{\rho_{\mathrm{L0}}^* U^* L^*} \equiv O(\varepsilon) \equiv \mu_{\mathrm{L}}\varepsilon, \tag{29}$$

$$\frac{G_{\mathrm{L}}^*}{\rho_{\mathrm{L0}}^* U^{*2}} \equiv O(1) \equiv G_{\mathrm{L}}, \tag{30}$$

$$\frac{K_{\mathrm{e,L}}^*}{\rho_{\mathrm{L0}}^* U^{*2}} \equiv O(1) \equiv K_{\mathrm{e,L}}, \tag{31}$$

$$\frac{\lambda_{\mathrm{relax,L}}^*}{T^*} \equiv O(\varepsilon) \equiv \lambda_{\mathrm{relax,L}}\varepsilon, \tag{32}$$

where T^* is the typical period of the wave, which can be related to the wavelength L^* and wave speed U^* as $U^* = L^*/T^*$.

The nondimensionalization of the energy equation (22) is as in Refs. [10,94]:

$$\frac{3(\kappa-1)\lambda_G^*}{p_{G0}^*\omega^* R_0^*}\frac{5}{4}\frac{T_0^*}{R_0^*} = \lambda_G\varepsilon, \tag{33}$$

where λ_G is the dimensionless constant of $O(1)$.

2.4. Multiple scales analysis

The independent variables t^*, x^*, r^*, y^*, and z^* are nondimensionalized as

$$t = \frac{t^*}{T^*}, \quad x = \frac{x^*}{L^*}, \quad r = \frac{r^*}{L^*}, \quad y = \frac{y^*}{L^*}, \quad z = \frac{z^*}{L^*}. \tag{34}$$

Next, t and x are extended to the near and far fields using the dimensionless wave amplitude ε [121]:

$$t_0 = t, \quad x_0 = x \quad \text{(near field)}, \tag{35}$$

$$t_1 = \varepsilon t, \quad x_1 = \varepsilon x \quad \text{(far field)}. \tag{36}$$

By the assumption of weakly diffracted waves in (2), the dependence of unknown variables on the radial direction (r,y,z) is smaller than that on the propagative direction x [88–90,93]. Then, the spatial coordinates r, y, and z are defined in the far field only as

$$r_{1/2} = \sqrt{\varepsilon}\Gamma_r r, \quad y_{1/2} = \sqrt{\varepsilon}\Gamma_y y, \quad z_{1/2} = \sqrt{\varepsilon}\Gamma_z z \quad \text{(far field)}. \tag{37}$$

For (37), the following relationships are introduced [88–90,93]:

$$\begin{aligned} r &= \frac{a_r^*}{L^*}\frac{r^*}{a_r^*} = \frac{r_{1/2}}{\sqrt{\varepsilon}\Gamma_r} \quad \left(r_{1/2} \equiv \frac{r^*}{a_r^*}\right), \\ y &= \frac{a_y^*}{L^*}\frac{y^*}{a_y^*} = \frac{y_{1/2}}{\sqrt{\varepsilon}\Gamma_y} \quad \left(y_{1/2} \equiv \frac{y^*}{a_y^*}\right), \\ z &= \frac{a_z^*}{L^*}\frac{z^*}{a_z^*} = \frac{z_{1/2}}{\sqrt{\varepsilon}\Gamma_z} \quad \left(z_{1/2} \equiv \frac{z^*}{a_z^*}\right). \end{aligned} \tag{38}$$

All the unknown variables can be regarded as functions of the extended independent variables of (35)–(38). The derivative operators are expanded as follows [121]:

$$\frac{\partial}{\partial t} = \frac{\partial}{\partial t_0} + \varepsilon\frac{\partial}{\partial t_1}, \tag{39}$$

$$\frac{\partial}{\partial x} = \frac{\partial}{\partial x_0} + \varepsilon\frac{\partial}{\partial x_1}, \tag{40}$$

$$\frac{\partial}{\partial r} = \sqrt{\varepsilon}\Gamma_r\frac{\partial}{\partial r_{1/2}}, \quad \frac{\partial}{\partial y} = \sqrt{\varepsilon}\Gamma_y\frac{\partial}{\partial y_{1/2}}, \quad \frac{\partial}{\partial z} = \sqrt{\varepsilon}\Gamma_z\frac{\partial}{\partial z_{1/2}}. \tag{41}$$

The unknown variables are expanded as a power series of ε:

$$\frac{R^*}{R_0^*} = 1 + \varepsilon R_1 + \varepsilon^2 R_2 + O(\varepsilon^3), \tag{42}$$

$$\frac{T_G^*}{T_0^*} = 1 + \varepsilon T_{G1} + \varepsilon^2 T_{G2} + O(\varepsilon^3), \tag{43}$$

$$\frac{p_L^*}{\rho_{L0}^* U^{*2}} = p_{L0} + \varepsilon p_{L1} + \varepsilon^2 p_{L2} + O(\varepsilon^3), \tag{44}$$

$$\frac{q_L^*}{\rho_{L0}^* U^{*2}} = q_{L0} + \varepsilon q_{L1} + \varepsilon^2 q_{L2} + O(\varepsilon^3), \tag{45}$$

$$\frac{u_x^*}{U^*} = \varepsilon u_{x1} + \varepsilon^2 u_{x2} + O(\varepsilon^3), \tag{46}$$

$$\frac{u_r^*}{U^*} = \varepsilon^{3/2} u_{r1} + \varepsilon^{5/2} u_{r2} + O(\varepsilon^{7/2}), \tag{47}$$

$$\frac{u_y^*}{U^*} = \varepsilon^{3/2} u_{y1} + \varepsilon^{5/2} u_{y2} + O(\varepsilon^{7/2}), \tag{48}$$

$$\frac{u_z^*}{U^*} = \varepsilon^{3/2} u_{z1} + \varepsilon^{5/2} u_{z2} + O(\varepsilon^{7/2}), \tag{49}$$

where u_x^*, u_r^*, u_y^*, and u_z^* are the components of velocity vector $\boldsymbol{u}^*$ in the x^*, r^*, y^*, and z^* directions, respectively. The magnitudes of u_r^*, u_y^*, and u_z^* are assumed to be smaller than that of the u_x^* direction [10,88,89,90,93]. Then, the expansions of u_r^*, u_y^*, and u_z^* begin with a higher order than that of u_x^* in (46)–(49). The components of displacement vector $\boldsymbol{d}^*$ are expanded in the same manner as $\boldsymbol{u}^*$:

$$\frac{d_x^*}{L^*} = \varepsilon d_{x1} + \varepsilon^2 d_{x2} + O(\varepsilon^3), \tag{50}$$

$$\frac{d_r^*}{L^*} = \varepsilon^{3/2} d_{r1} + \varepsilon^{5/2} d_{r2} + O(\varepsilon^{7/2}), \tag{51}$$

$$\frac{d_y^*}{L^*} = \varepsilon^{3/2} d_{y1} + \varepsilon^{5/2} d_{y2} + O(\varepsilon^{7/2}), \tag{52}$$

$$\frac{d_z^*}{L^*} = \varepsilon^{3/2} d_{z1} + \varepsilon^{5/2} d_{z2} + O(\varepsilon^{7/2}). \tag{53}$$

The components of the deviatoric stress tensor $\boldsymbol{\tau}^*$ are expanded as

$$\frac{\tau_{xx}^*}{\rho_{L0}^* U^{*2}} = \varepsilon\tau_{xx1} + \varepsilon^2\tau_{xx2} + O(\varepsilon^3), \tag{54}$$

$$\frac{\tau_{xr}^*}{\rho_{L0}^* U^{*2}} = \varepsilon^{3/2}\tau_{xr1} + \varepsilon^{5/2}\tau_{xr2} + O(\varepsilon^{7/2}), \tag{55}$$

$$\frac{\tau_{xy}^*}{\rho_{L0}^* U^{*2}} = \varepsilon^{3/2}\tau_{xy1} + \varepsilon^{5/2}\tau_{xy2} + O(\varepsilon^{7/2}), \tag{56}$$

$$\frac{\tau_{xz}^*}{\rho_{L0}^* U^{*2}} = \varepsilon^{3/2}\tau_{xz1} + \varepsilon^{5/2}\tau_{xz2} + O(\varepsilon^{7/2}), \tag{57}$$

where other components that do not affect the result are omitted.

The gas density is assumed to be significantly smaller than the liquid density in the initial state:

$$\frac{\rho_{G0}^*}{\rho_{L0}^*} \equiv O(\varepsilon^3). \tag{58}$$

The dimensionless liquid pressure is defined as

$$p_{L0} = \frac{p_{L0}^*}{\rho_{L0}^* U^{*2}} \equiv O(1). \tag{59}$$

The liquid density is expanded as [92]

$$\frac{\rho_L^*}{\rho_{L0}^*} = 1 + \varepsilon^2\rho_{L1} + \varepsilon^3\rho_{L2} + O(\varepsilon^4), \tag{60}$$

where the first order of the expansion is determined using (23), (27), and (44).

To incorporate the weak nonuniformity of the spatial distribution of bubbles in the initial state, void fraction α is expanded as [10,88–90,93]

$$\frac{\alpha}{\alpha_0} = 1 + \varepsilon[\alpha_1 + \delta(x_1)] + \varepsilon^2\alpha_2 + O(\varepsilon^3), \tag{61}$$

where δ is the known variable that represents the spatial nonuniformity of the void fraction in the initial state. The effect of the spatial nonuniformity of the void fraction is assumed to appear only in the far field; then, δ is the function of x_1 only [10,88–90,93].

3. Results of theoretical analysis

The scale parameters (25)–(33), derivative operators (39)–(41), and expansions of the unknown variables (42)–(61) are substituted into basic equations (11)–(24).

3.1. Approximation of first order

From the approximations of $O(\varepsilon)$, linear equations are obtained for (11)–(24), as follows:

$$\frac{\partial\alpha_1}{\partial t_0} - 3\frac{\partial R_1}{\partial t_0} + \frac{\partial u_{x1}}{\partial x_0} = 0, \tag{62}$$

$$\alpha_0\frac{\partial\alpha_1}{\partial t_0} - (1-\alpha_0)\frac{\partial u_{x1}}{\partial x_0} = 0, \tag{63}$$

$$(1-\alpha_0)\frac{\partial u_{x1}}{\partial t_0} + \frac{\partial p_{\mathrm{L}1}}{\partial x_0} - \frac{\partial \tau_{xx1}}{\partial x_0} - \left(K_{\mathrm{e,L}} - \frac{2}{3}G_{\mathrm{L}}\right)\frac{\partial^2 d_{x1}}{\partial x_0^2} = 0, \tag{64}$$

$$\frac{\partial T_{\mathrm{G}1}}{\partial t_0} + 3(\kappa-1)\frac{\partial R_1}{\partial t_0} = 0, \tag{65}$$

$$p_{\mathrm{G}0}T_{\mathrm{G}1} - p_{\mathrm{L}1} + 3(\kappa-1)p_{\mathrm{G}0}R_1 - \frac{\Delta^2}{\Omega^2}R_1 = 0, \tag{66}$$

$$\tau_{xx1} - 2G_{\mathrm{L}}\frac{\partial d_{x1}}{\partial x_0} = 0. \tag{67}$$

The velocity and displacement are related by (14) as

$$u_{x1} = \frac{\partial d_{x1}}{\partial t_0}. \tag{68}$$

From the approximation of the Keller–Miksis equation (17), the linear natural frequency of bubble oscillation ω_{B}^* is obtained:

$$\omega_{\mathrm{B}}^* = \sqrt{\frac{3\kappa p_{\mathrm{G}0}^* - 2\sigma^*/R_0^* + 4G_{\mathrm{L}}^*}{\rho_{\mathrm{L}0}^* R_0^{*2}}}. \tag{69}$$

In (69), the effect of liquid elasticity at the bubble–liquid interface [91] is introduced to our previous works [88,93–95]. Note that ω_{B}^* of (69) is obtained from the linear approximation, then the actual frequency of bubble oscillation will be shifted by accumulation of nonlinearity and wave amplitude [122,123]. In addition, bubble–bubble interaction [39,44,46,104–106] and dual frequency ultrasound [129–131] also affect the frequency of bubble oscillation, however these are not considered in this study.

Equations (62)–(67) are combined into a single equation of R_1 as

$$\frac{\partial^2 R_1}{\partial t_0^2} - v_{\mathrm{P}}^2\frac{\partial^2 R_1}{\partial x_0^2} = 0, \tag{70}$$

where the phase velocity v_{P} is given by

$$v_{\mathrm{P}} = \sqrt{\frac{\Delta^2/\Omega^2 + 3\alpha_0\left(K_{\mathrm{e,L}} + 4G_{\mathrm{L}}/3\right)}{3\alpha_0(1-\alpha_0)}}. \tag{71}$$

For simplicity, $v_{\mathrm{P}} \equiv 1$ is imposed and the typical wave speed U^* is given by

$$U^* = \sqrt{\frac{\omega_{\mathrm{B}}^{*2}R_0^{*2}\rho_{\mathrm{L}0}^* + 3\alpha_0\left(K_{\mathrm{e,L}}^* + 4G_{\mathrm{L}}^*/3\right)}{3\alpha_0(1-\alpha_0)\rho_{\mathrm{L}0}^*}}. \tag{72}$$

In (72), the effect of the elasticity of the entire liquid is newly introduced to our previous works [88,93–95].

Next, the variable transformation is introduced as

$$\phi_0 = t_0 - x_0. \tag{73}$$

Then, the equation describing the right-running waves is obtained:

$$\frac{\partial f}{\partial t_0} + \frac{\partial f}{\partial x_0} = 0. \tag{74}$$

The variable transformation (73) is introduced into approximated equations (62)–(68), and all unknown variables are written in terms of $R_1 = f$ as follows:

$$\begin{aligned} &\alpha_1 = s_1 f, \quad u_{x1} = s_2 f, \quad T_{\mathrm{G}1} = s_3 f, \\ &p_{\mathrm{L}1} = s_4 f, \quad d_{x1} = s_5\int f\,\mathrm{d}\phi_0, \quad \tau_{xx1} = s_6 f, \end{aligned} \tag{75}$$

where

$$s_1 = 3(1-\alpha_0), \tag{76}$$

$$s_2 = -3\alpha_0, \tag{77}$$

$$s_3 = -3(\kappa-1), \tag{78}$$

$$s_4 = 3\alpha_0\left(K_{\mathrm{e,L}} + \frac{4}{3}G_{\mathrm{L}}\right) - 3\alpha_0(1-\alpha_0), \tag{79}$$

$$s_5 = -3\alpha_0, \tag{80}$$

$$s_6 = 6\alpha_0 G_{\mathrm{L}}. \tag{81}$$

3.2. Approximation of radial direction

From the approximations of $O(\varepsilon^{3/2})$, the radial components of the momentum conservation equation (13) are

$$(1-\alpha_0)\frac{\partial u_{r1}}{\partial t_0} + \Gamma_r\frac{\partial p_{\mathrm{L}1}}{\partial r_{1/2}} - \frac{\partial \tau_{xr1}}{\partial x_0} - \left(K_{\mathrm{e,L}} - \frac{2}{3}G_{\mathrm{L}}\right)\Gamma_r\frac{\partial^2 d_{x1}}{\partial x_0\partial r_{1/2}} = 0, \tag{82}$$

$$(1-\alpha_0)\frac{\partial u_{y1}}{\partial t_0} + \Gamma_y\frac{\partial p_{\mathrm{L}1}}{\partial y_{1/2}} - \frac{\partial \tau_{xy1}}{\partial x_0} - \left(K_{\mathrm{e,L}} - \frac{2}{3}G_{\mathrm{L}}\right)\Gamma_y\frac{\partial^2 d_{x1}}{\partial x_0\partial y_{1/2}} = 0, \tag{83}$$

$$(1-\alpha_0)\frac{\partial u_{z1}}{\partial t_0} + \Gamma_z\frac{\partial p_{\mathrm{L}1}}{\partial z_{1/2}} - \frac{\partial \tau_{xz1}}{\partial x_0} - \left(K_{\mathrm{e,L}} - \frac{2}{3}G_{\mathrm{L}}\right)\Gamma_z\frac{\partial^2 d_{x1}}{\partial x_0\partial z_{1/2}} = 0. \tag{84}$$

The components of the deviatoric stress tensor (16) related to the radial directions are

$$\tau_{xr1} - G_{\mathrm{L}}\frac{\partial d_{r1}}{\partial x_0} - G_{\mathrm{L}}\Gamma_r\frac{\partial d_{x1}}{\partial r_{1/2}} = 0, \tag{85}$$

$$\tau_{xy1} - G_{\mathrm{L}}\frac{\partial d_{y1}}{\partial x_0} - G_{\mathrm{L}}\Gamma_y\frac{\partial d_{x1}}{\partial y_{1/2}} = 0, \tag{86}$$

$$\tau_{xz1} - G_{\mathrm{L}}\frac{\partial d_{z1}}{\partial x_0} - G_{\mathrm{L}}\Gamma_z\frac{\partial d_{x1}}{\partial z_{1/2}} = 0. \tag{87}$$

The velocity and displacement are related by (14) as

$$u_{r1} = \frac{\partial d_{r1}}{\partial t_0}, \quad u_{y1} = \frac{\partial d_{y1}}{\partial t_0}, \quad u_{z1} = \frac{\partial d_{z1}}{\partial t_0}. \tag{88}$$

The variable transformation (73) is introduced into (82)–(88):

$$\frac{\partial u_{r1}}{\partial \phi_0} = 3\alpha_0 \Gamma_r \frac{\partial f}{\partial r_{1/2}}, \tag{89}$$

$$\frac{\partial u_{y1}}{\partial \phi_0} = 3\alpha_0 \Gamma_y \frac{\partial f}{\partial y_{1/2}}, \tag{90}$$

$$\frac{\partial u_{z1}}{\partial \phi_0} = 3\alpha_0 \Gamma_z \frac{\partial f}{\partial z_{1/2}}, \tag{91}$$

where the forms of (89)–(91) are the same as in our previous work [93].

3.3. Approximation of second order

From the approximations of $O(\varepsilon^2)$, the following equations are obtained for (11)–(24) as

$$\frac{\partial \alpha_2}{\partial t_0} - 3\frac{\partial R_2}{\partial t_0} + \frac{\partial u_{x2}}{\partial x_0} = K_1, \tag{92}$$

$$\alpha_0 \frac{\partial \alpha_2}{\partial t_0} - (1-\alpha_0)\frac{\partial u_{x2}}{\partial x_0} = K_2, \tag{93}$$

$$(1-\alpha_0)\frac{\partial u_{x2}}{\partial t_0} + \frac{\partial p_{L2}}{\partial x_0} - \frac{\partial \tau_{xx2}}{\partial x_0} - \left(K_{e,L} - \frac{2}{3}G_L\right)\frac{\partial^2 d_{x2}}{\partial x_0^2} = K_3, \tag{94}$$

$$\frac{\partial T_{G2}}{\partial t_0} + 3(\kappa - 1)\frac{\partial R_2}{\partial t_0} = K_4, \tag{95}$$

$$p_{G0} T_{G2} - p_{L2} + 3(\kappa - 1) p_{G0} R_2 - \frac{\Delta^2}{\Omega^2} R_2 = K_5, \tag{96}$$

$$\tau_{xx2} - 2G_L \frac{\partial d_{x2}}{\partial x_0} = K_6. \tag{97}$$

The explicit forms of the inhomogeneous terms $K_i\,(i = 1, \ldots, 6)$ are shown in Appendix A. Equations (92)–(97) are combined into a single equation:

$$\frac{\partial^2 R_2}{\partial t_0^2} - \frac{\partial^2 R_2}{\partial x_0^2} = K. \tag{98}$$

The inhomogeneous term K is given by

$$\begin{aligned} K = &-\frac{1}{3}\frac{\partial K_1}{\partial t_0} + \frac{1}{3(1-\alpha_0)}\left(K_{e,L} + \frac{4}{3}G_L\right)\int \frac{\partial^2 K_1}{\partial x_0^2} dt_0 + \frac{1}{3\alpha_0}\frac{\partial K_2}{\partial t_0} \\ &- \frac{1}{3\alpha_0(1-\alpha_0)}\left(K_{e,L} + \frac{4}{3}G_L\right)\int \frac{\partial^2 K_2}{\partial x_0^2} dt_0 + \frac{1}{3\alpha_0(1-\alpha_0)}\frac{\partial K_3}{\partial x_0} \\ &- \frac{p_{G0}}{3\alpha_0(1-\alpha_0)}\int \frac{\partial^2 K_4}{\partial x_0^2} \mathrm{d}t_0 + \frac{1}{3\alpha_0(1-\alpha_0)}\frac{\partial^2 K_5}{\partial x_0^2} + \frac{1}{3\alpha_0(1-\alpha_0)}\frac{\partial^2 K_6}{\partial x_0^2}. \end{aligned} \tag{99}$$

As the solvable condition for (98), $K = 0$ is imposed [88–90,92], and the following relation is obtained for 2D and 3D spatial cases:

$$\begin{aligned} &2\frac{\partial}{\partial \phi_0}\left[\frac{\partial f}{\partial x_1} + \frac{\partial f}{\partial t_1} + \Pi_{02}\frac{\partial f}{\partial t_1} + \Pi_{01}\frac{\partial f}{\partial \phi_0} + \Pi_4 \delta(x_1)\frac{\partial f}{\partial \phi_0} + \Pi_1 f \frac{\partial f}{\partial \phi_0} + \Pi_{21}\frac{\partial^2 f}{\partial \phi_0^2} \right. \\ &\left. + \Pi_{22} f + \Pi_3 \frac{\partial^3 f}{\partial \phi_0^3}\right] \\ &= \begin{cases} \Gamma_r^2\left(\dfrac{1}{r_{1/2}}\dfrac{\partial f}{\partial r_{1/2}} + \dfrac{\partial^2 f}{\partial r_{1/2}^2}\right) & \text{(for 2D case)}, \\ \Gamma_y^2 \dfrac{\partial f}{\partial y_{1/2}^2} + \Gamma_z^2 \dfrac{\partial f}{\partial z_{1/2}^2} & \text{(for 3D case)}. \end{cases} \end{aligned} \tag{100}$$

The derivative operators (39)–(41), equation of the near field (74), equations of the radial direction (89)–(91), and (100) are combined:

$$\begin{aligned} &\frac{\partial}{\partial t}\left\{\frac{\partial f}{\partial x} + \frac{\partial f}{\partial t} + \Pi_{02}\frac{\partial f}{\partial t} + \varepsilon\left[\Pi_{01}\frac{\partial f}{\partial t} + \Pi_4 \delta(x_1)\frac{\partial f}{\partial t} + \Pi_1 f \frac{\partial f}{\partial t} + \Pi_{21}\frac{\partial^2 f}{\partial t^2} + \Pi_{22} f \right.\right. \\ &\left.\left. + \Pi_3 \frac{\partial^3 f}{\partial t^3}\right]\right\} \\ &= \begin{cases} \dfrac{1}{2}\left(\dfrac{1}{r}\dfrac{\partial f}{\partial r} + \dfrac{\partial^2 f}{\partial r^2}\right) & \text{(for 2D case)}, \\ \dfrac{1}{2}\left(\dfrac{\partial^2 f}{\partial y^2} + \dfrac{\partial^2 f}{\partial z^2}\right) & \text{(for 3D case)}. \end{cases} \end{aligned} \tag{101}$$

Finally, the KZK equation is obtained:

$$\frac{\partial}{\partial \tau}\left(\frac{\partial f}{\partial X} + \Pi_1 f \frac{\partial f}{\partial \tau} + \Pi_{21}\frac{\partial^2 f}{\partial \tau^2} + \Pi_{22} f + \Pi_3 \frac{\partial^3 f}{\partial \tau^3}\right) = \Delta_\perp f, \tag{102}$$

where $\Delta_\perp$ is the Laplacian operator given for 2D and 3D spatial cases by

$$\Delta_\perp f = \begin{cases} \dfrac{\Gamma_r^2}{2}\left(\dfrac{1}{R}\dfrac{\partial f}{\partial R} + \dfrac{\partial^2 f}{\partial R^2}\right) & \text{(for 2D case)}, \\ \dfrac{1}{2}\left(\Gamma_y^2 \dfrac{\partial^2 f}{\partial Y^2} + \Gamma_z^2 \dfrac{\partial^2 f}{\partial Z^2}\right) & \text{(for 3D case)}. \end{cases} \tag{103}$$

The following variable transformations are used:

$$\tau = t - \{1 + \Pi_{02} + \varepsilon[\Pi_{01} + \Pi_4 \delta(x_1)]\}x, \tag{104}$$

$$X = \varepsilon x, \tag{105}$$

$$\begin{cases} R = \sqrt{\varepsilon}\,\Gamma_r r & \text{(for 2D case)}, \\ Y = \sqrt{\varepsilon}\,\Gamma_y y,\ Z = \sqrt{\varepsilon}\,\Gamma_z z & \text{(for 3D case)}, \end{cases} \tag{106}$$

where τ is the retarded time. In the KZK equation (102), the right-hand side with the Laplacian operator represents the diffraction (focusing) effect.

3.4. Coefficients of KZK equation

Advection coefficients Π_{01}, Π_{02}, and Π_4 are given by

$$\Pi_{01} = \left[1 - \alpha_0 - \left(K_{e,L} + \frac{4}{3}G_L\right)\right]^2 \frac{V^2}{2}, \tag{107}$$

$$\Pi_{02} = -\left(K_{e,L} + \frac{4}{3}G_L\right)\frac{1}{2(1-\alpha_0)}, \tag{108}$$

$$\Pi_4 = \frac{1 - 2\alpha_0}{2(1-\alpha_0)} - \left(K_{e,L} + \frac{4}{3}G_L\right)\frac{1}{2(1-\alpha_0)}. \tag{109}$$

By the effect of the elasticity of the entire liquid, the new coefficient Π_{02} is introduced in this study and terms are added to Π_{01} and Π_4 from our previous work [10]. The spatial nonuniformity of the initial bubble distribution $\delta(x_1)$ only appears in the variable transformation (104), in which it only affects the advection term [88–90,93]. Nonlinear coefficient Π_1 is given by

$$\begin{aligned} \Pi_1 = \frac{1}{6}\left[k_1 - \frac{1}{1-\alpha_0}\left(K_{e,L} + \frac{4}{3}G_L\right)k_1 - \frac{k_2}{\alpha_0} + \frac{1}{1-\alpha_0}\left(K_{e,L} + \frac{4}{3}G_L\right)\frac{k_2}{\alpha_0} \right. \\ \left. + \frac{k_3}{\alpha_0(1-\alpha_0)} + \frac{p_{G0}k_4}{\alpha_0(1-\alpha_0)} + \frac{k_5}{\alpha_0(1-\alpha_0)} + \frac{k_6}{\alpha_0(1-\alpha_0)}\right], \end{aligned} \tag{110}$$

where

$$k_1 = -6(2 - s_1) - 2s_2(3 - s_1), \tag{111}$$

$$k_2 = 2\alpha_0 s_1 s_2, \tag{112}$$

$$k_3 = 0, \tag{113}$$

$$k_4 = -3(\kappa - 1)(3\kappa - 4 + 2s_3), \tag{114}$$

$$k_5 = \left[8G_{\mathrm{L}} - 6(\kappa - 2)p_{\mathrm{G0}} + 2\frac{\Delta^2}{\Omega^2}\right] - 6p_{\mathrm{G0}}s_3, \tag{115}$$

$$k_6 = 0. \tag{116}$$

Dissipation coefficient Π_{21} is divided into five terms for each factor and region:

$$\Pi_{21} = \underbrace{\Pi_{\mathrm{C}}}_{\substack{\text{liquid}\\ \text{compressibility}}} + \underbrace{\Pi_{\mathrm{v,E}}}_{\substack{\text{viscosity of}\\ \text{entire liquid}}} + \underbrace{\Pi_{\mathrm{v,I}}}_{\substack{\text{liquid viscosity of}\\ \text{bubble–liquid interface}}} + \underbrace{\Pi_{\mathrm{e,E}}}_{\substack{\text{elasticity of}\\ \text{entire liquid}}} + \underbrace{\Pi_{\mathrm{e,I}}}_{\substack{\text{liquide lasticity of}\\ \text{bubble–liquid interface}}}, \tag{117}$$

where

$$\Pi_{\mathrm{C}} = -\frac{V\Delta}{2} < 0, \tag{118}$$

$$\Pi_{\mathrm{v,E}} = -\frac{2\mu_{\mathrm{L}}}{3(1-\alpha_0)} < 0, \tag{119}$$

$$\Pi_{\mathrm{v,I}} = -\frac{2\mu_{\mathrm{L}}}{3\alpha_0(1-\alpha_0)} < 0, \tag{120}$$

$$\Pi_{\mathrm{e,E}} = \frac{V\Delta}{2(1-\alpha_0)}\left(K_{\mathrm{e,L}} + \frac{4}{3}G_{\mathrm{L}}\right) + \frac{\lambda_{\mathrm{relax,L}}G_{\mathrm{L}}}{1-\alpha_0} > 0, \tag{121}$$

$$\Pi_{\mathrm{e,I}} = \frac{2\lambda_{\mathrm{relax,L}}G_{\mathrm{L}}}{3\alpha_0(1-\alpha_0)} > 0. \tag{122}$$

Further, Π_{22} and Π_3 are the dissipation and dispersion coefficients, respectively, given by

$$\Pi_{22} = \frac{p_{\mathrm{G0}}(\kappa - 1)}{2\alpha_0(1-\alpha_0)}\lambda_{\mathrm{G}}, \tag{123}$$

$$\Pi_3 = -\frac{\Delta^2}{6\alpha_0(1-\alpha_0)}. \tag{124}$$

Whereas Π_{21} depends on the compressibility, viscosity, and elasticity of the liquid phase, Π_{22} depends on the thermal conductivity of the gas phase.

3.5. Effects of elasticity

Fig. 3 shows the coefficients for cases in which the liquid phase is water (black) and liver tissue (red). The properties of the water and liver tissue used in the calculations are shown in Table 1. Unless otherwise stated, these values are used in all calculations in Sections 3.5, 3.6, 3.7, and 4. As shown in Fig. 3, elasticity decreases the magnitudes of the nonlinear coefficient Π_1, dissipation coefficients Π_{21} and Π_{22}, and dispersion coefficient Π_3, and increases the phase velocity U^* and linear natural frequency of bubble oscillation ω_{B}^*. Decrease of nonlinearity by the liquid elasticity is qualitatively consistent with the previous result [34] focusing of single bubble behavior.

3.6. Comparison of three viscoelastic models

In Fig. 4, the three viscoelastic models; Zener model, Maxwell model, and Kelvin–Voigt model are compared. The Zener model, that are the rigidity $G_{\mathrm{L}}^* \neq 0$ and the relaxation time $\lambda_{\mathrm{relax,L}}^* \neq 0$, corresponds to the generalization of the Maxwell model ($G_{\mathrm{L}}^* = 0$) and the Kelvin–Voigt model ($\lambda_{\mathrm{relax,L}}^* = 0$). From the Fig. 4b, the magnitude of the dissipation coefficient Π_{21} is decreased in case of the Zener model compare to the

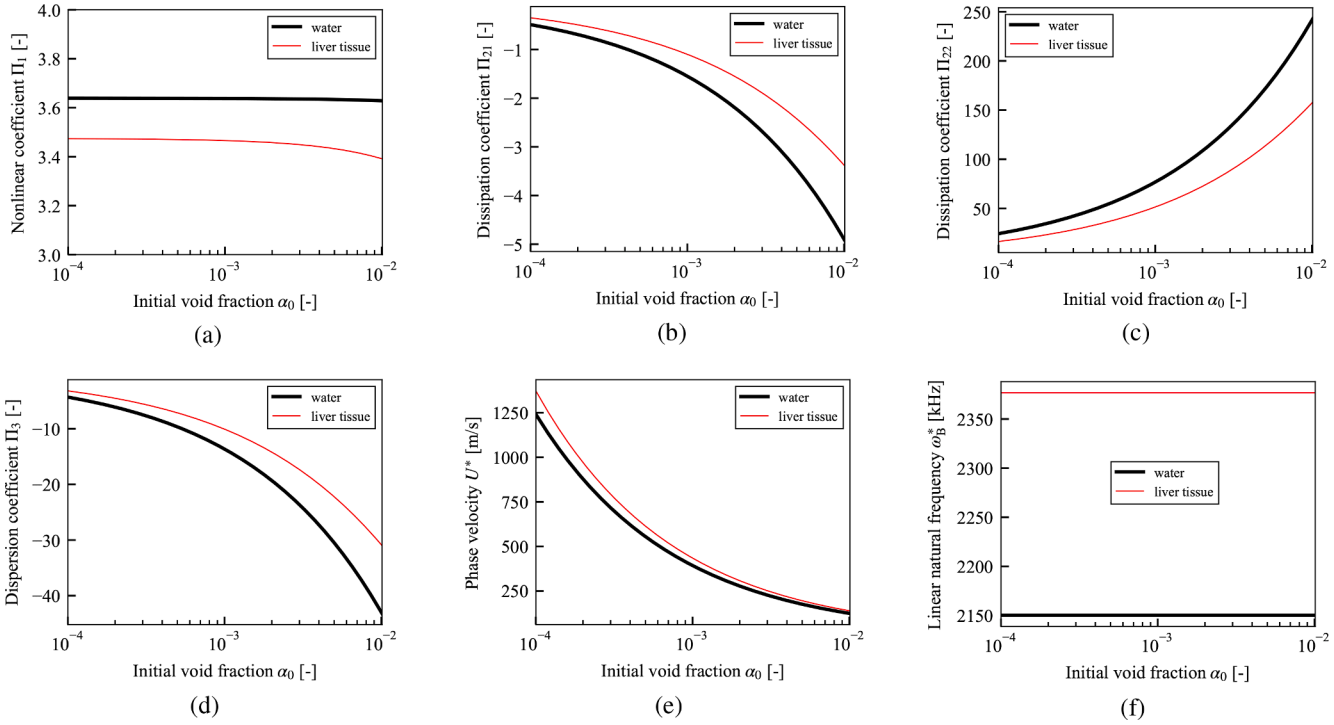

Fig. 3. (a) Nonlinear coefficient Π_1, (b) and (c) dissipation coefficients Π_{21} and Π_{22}, (d) dispersion coefficient Π_3, (e) phase velocity U^*, and (f) linear natural frequency of bubble oscillation ω_{B}^*, versus initial void fraction α_0. The black and red lines indicate cases in which the liquid phase is water and liver tissue, respectively. The material properties of water and liver tissue are shown in Table 1. Parameters: initial bubble radius $R_0^* = 10\,\mu$m, frequency of sound source $f^* = 100$ kHz, pressure amplitude of sound source $p_0^* = 100$ kPa, initial liquid pressure $p_{\mathrm{L0}}^* = 101325$ Pa, and initial temperature of gas and liquid phases $T_0^* = 36.0$ °C. The gas inside the bubble is air with the ratio of specific heats $\kappa = 1.4$ and thermal conductivity $\lambda_{\mathrm{G}}^* = 0.025$ W/(m·K).

Table 1
Physical properties of liquid phase.

	Water	Liver tissue [47,128]
Rigidity G_L^* [kPa]	0	40
Poisson's ratio ν_L [-]	-	0.45
Relaxation time $\lambda_{relax,L}^*$ [s]	0	3.0×10^{-9}
Viscosity μ_L^* [Pa·s]	0.001	0.001
Surface tension σ^* [N/m]	0.056	0.056
Density ρ_{L0}^* [kg/m^3]	998	1100
Sound speed c_{L0}^* [m/s]	1486	1549

Kelvin–Voigt model. Then, the relaxation time of the liquid phase decrease the dissipation of the ultrasound. This result is qualitatively consistent with the result for the case of single bubble by Warnez and Johnsen [42] that incorporating the relaxation time increases bubble growth. However, all parameters shown in Fig. 4 are almost affected by the generalization from the Maxwell model to the Zener model. Hence, the effect of rigidity G_L^* is quite larger than that of the relaxation time $\lambda_{relax,L}^*$ for all parameters.

3.7. Comparison of elasticity of entire liquid and bubble–liquid interface

In Fig. 5, the effects of the liquid elasticity of the entire liquid and bubble–liquid interface are compared. As the effects of each factor become larger, the red (elasticity of entire liquid) and blue (elasticity of bubble–liquid interface) lines differ from the black line (both elasticities not considered).

As shown in Fig. 5, the nonlinear coefficient Π_1 is decreased by both elasticities; the effect of the bubble–liquid interface is large at the wide range of the initial void fraction α_0, while the effect of the entire liquid gradually increases as the value of α_0 increases. The magnitudes of the dissipation coefficients Π_{21} and Π_{22} and the dispersion coefficient Π_3 are affected by the elasticity of the bubble–liquid interface, whereas the effect of the elasticity of the entire liquid is only slight and increases with the initial void fraction α_0. The phase velocity U^* and linear natural frequency of the bubble oscillation ω_B^* increase when the elasticity of the bubble–liquid interface is considered, whereas the effects of the elasticity of the entire liquid are not observed.

3.8. Limitation of KZK equation (102)

The resultant KZK equation (102) includes the nonlinear term with coefficient Π_1 owing to nonlinearity of ultrasound propagation, while the dissipation and dispersion terms are limited to linear form. However, effects of nonlinear dissipation [124–127] will become large particularly in case of high amplitude. Two main methods to incorporate the nonlinear dissipation are (i) extending to over third order analysis from the second order of this study, (ii) nondimensionalization with lower order of $\varepsilon(\ll 1)$ for liquid viscosity of (29). These extensions will significantly change the framework of theoretical analysis and the resultant equation will be no longer the form of original KZK equation, but be very important for practical applications then be presented in our future work.

4. Numerical example

4.1. Method

The KZK equation of the spatial 2D form of (102) is numerically solved. As in our previous work [10], the finite-difference time-domain scheme [57,58] is used, which has been widely used to simulate focused ultrasound in single phase liquid [57–68]. To solve the fluctuation of liquid pressure p_{L1}, the KZK equation (102) is rewritten using the relation of the fluctuation of bubble radius f and liquid pressure p_{L1} in (75):

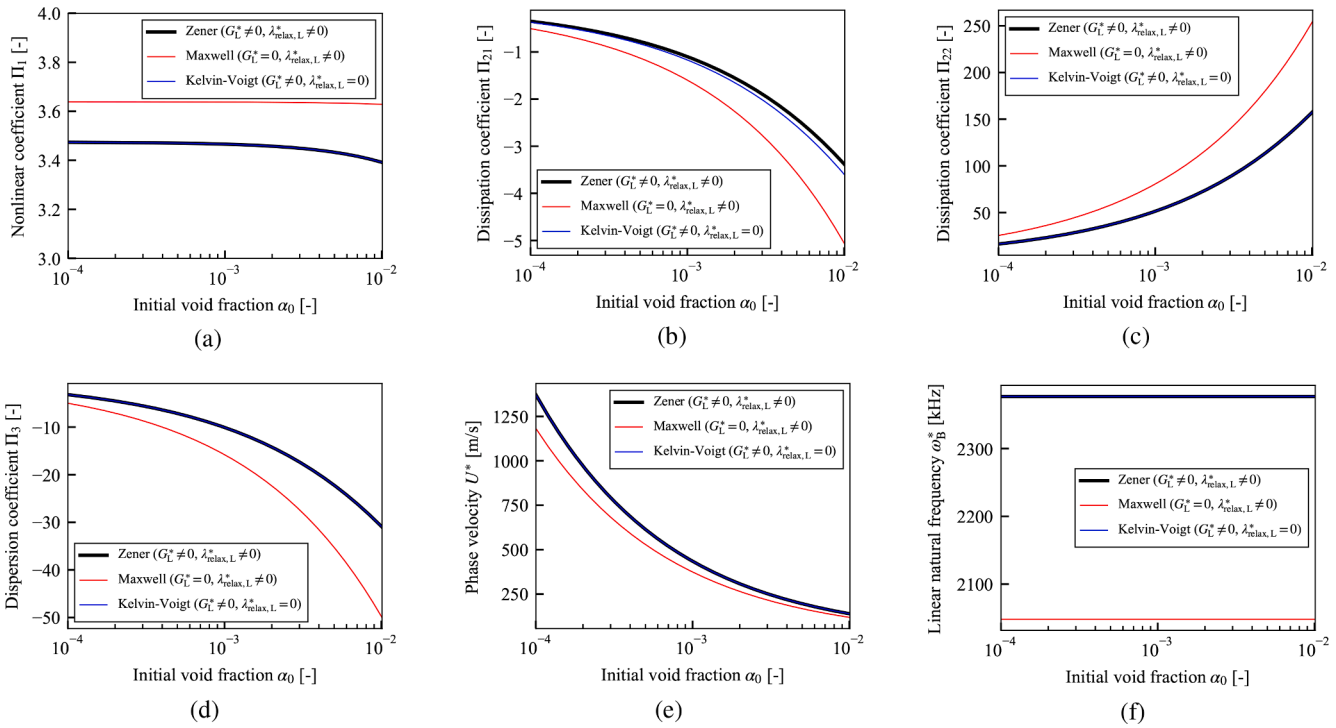

Fig. 4. The same parameters as in Fig. 3 are shown for the case of liver tissue. The black line represents the case in which the viscoelastic model is the Zener model ($G_L^* \neq 0$ and $\lambda_{relax,L}^* \neq 0$), the red line represents the case of the Maxwell model ($G_L^* = 0$ and $\lambda_{relax,L}^* \neq 0$), and the blue line represents the case of Kelvin–Voigt model ($G_L^* \neq 0$ and $\lambda_{relax,L}^* = 0$). The other conditions are same as in Fig. 3.

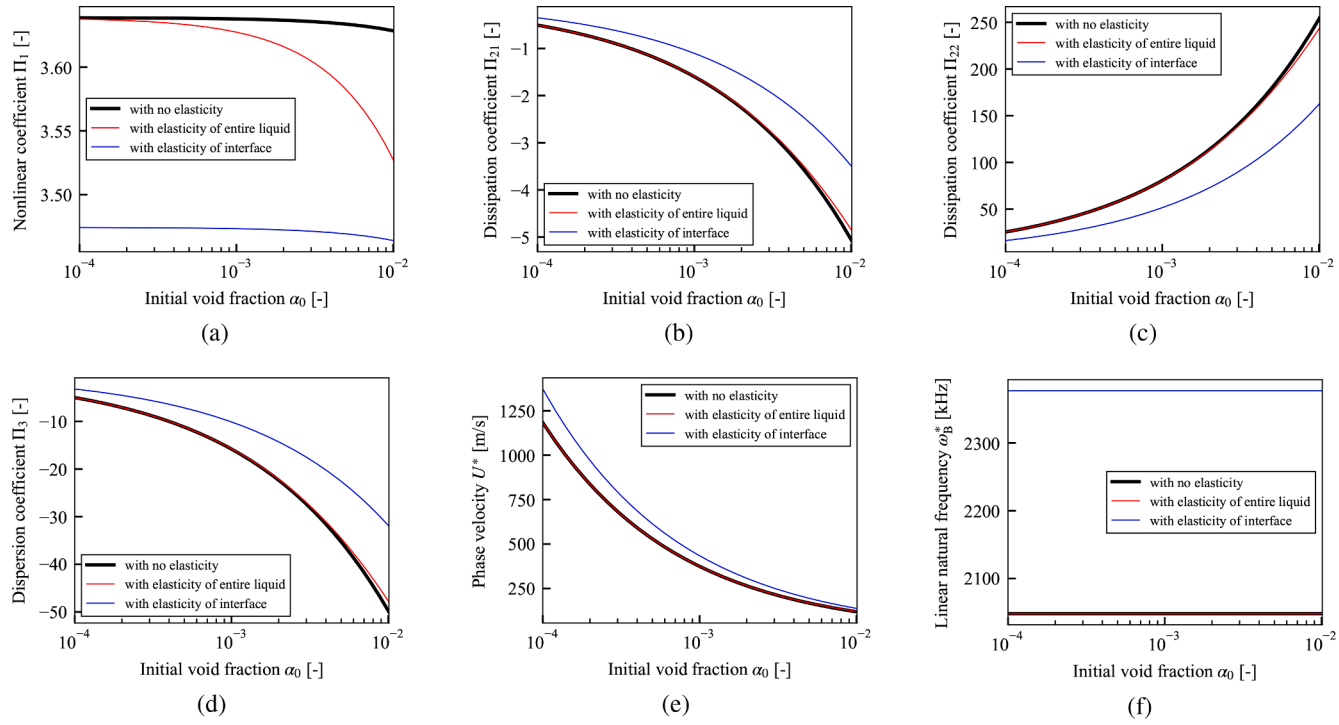

Fig. 5. The same parameters as in Fig. 3 are shown for the case of liver tissue. The black line represents the case in which both elasticities are not considered. The red line represents the case in which only the elasticity of the entire liquid is considered, and the blue line represents the case in which only the elasticity of the bubble–liquid interface is considered. The other conditions are same as in Fig. 3.

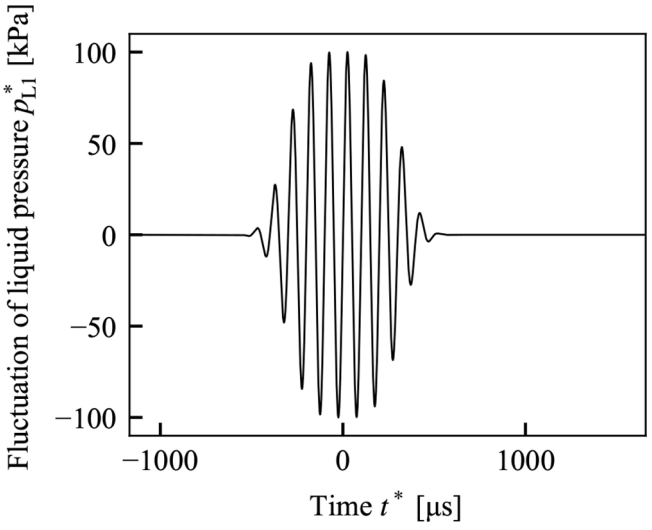

Fig. 6. Boundary condition for calculating Figs. 7 and 8 at the center of the sound source ($x^* = 0$ mm and $r^* = 0$ mm).

$$\frac{\partial p_{L1}}{\partial X} = \frac{1}{4G_r}\int_{-\infty}^{\tau}\left(\frac{\partial^2 p_{L1}}{\partial R^2}+\frac{1}{R}\frac{\partial p_{L1}}{\partial R}\right)d\tau - \frac{\Pi_1}{s_4}p_{L1}\frac{\partial p_{L1}}{\partial \tau} - \Pi_{21}\frac{\partial^2 p_{L1}}{\partial \tau^2} - \Pi_{22}p_{L1} - \Pi_3\frac{\partial^3 p_{L1}}{\partial \tau^3}, \tag{125}$$

where the focusing gain G_r is given by

$$G_r = \frac{\omega^* a_r^{*2}}{2U^* d_f^*}. \tag{126}$$

The variable transformations (104)–(106) are rewritten again as

$$\tau = \omega^*\left(t^* - \{1+\Pi_{02}+\varepsilon[\Pi_{01}+\Pi_4\delta(x_1)]\}\frac{x^*}{U^*}\right), \tag{127}$$

$$X = \frac{x^*}{d_f^*}, \tag{128}$$

$$R = \frac{r^*}{a_r^*}. \tag{129}$$

The step sizes of each direction are $\Delta\tau = 2\pi/240$, $\Delta X = 0.00025$, and $\Delta R = 0.01$, and the calculation regions are $\tau_{min} \leqq \tau \leqq \tau_{max}$, $0 \leqq X \leqq X_{max}$, and $0 \leqq R \leqq R_{max}$. To suppress the numerical oscillation, the calculation regions need to be sufficiently large for the direction of τ and R; then, $\tau_{min} = -(G_r + 24\pi)$, $\tau_{max} = 34\pi$, and $R_{max} = 4$ are set.

Next, the KZK equation (125) is split into three parts and solved term by term:

$$\frac{\partial p_{L1}}{\partial X} = \frac{1}{4G_r}\int_{-\infty}^{\tau}\left(\frac{\partial^2 p_{L1}}{\partial R^2}+\frac{1}{R}\frac{\partial p_{L1}}{\partial R}\right)d\tau, \tag{130}$$

$$\frac{\partial p_{L1}}{\partial X} = -\Pi_{21}\frac{\partial^2 p_{L1}}{\partial \tau^2} - \Pi_{22}p_{L1} - \Pi_3\frac{\partial^3 p_{L1}}{\partial \tau^3}, \tag{131}$$

$$\frac{\partial p_{L1}}{\partial X} = -\frac{\Pi_1}{s_4}p_{L1}\frac{\partial p_{L1}}{\partial \tau}. \tag{132}$$

The diffraction term of (130) is solved by the implicit backward finite difference (IBFD) method in the R direction with the truncation error of order $\Delta X + (\Delta\tau)^2 + \Delta R$. The dissipation and dispersion terms of (131) are also solved using the IBFD method in the τ direction. The second and third derivative terms of (131) are discretized using the central difference method [10,57,58]. The truncation error for solving (131) is of order $(\Delta X)^2 + (\Delta\tau)^2$. The nonlinear term of (132) is solved using the implicit analytical solution with an error of order $(\Delta\tau)^2$. In addition, the error caused by separately introducing the diffraction, dissipation,

dispersion, and nonlinear effects is of order $(\Delta X)^2$. The total error is estimated as $\Delta X+(\Delta\tau)^2+\Delta R$ [57,58].

The boundary condition at $X=0$ for the focused sound source is given by

$$p_{\mathrm{L1}}(X=0,\tau,R)=\begin{cases}\exp\left\{-\left[\dfrac{2(\tau+G_rR^2)}{T_{\mathrm{d}}}\right]^m\right\}\dfrac{p_0^*}{\varepsilon\rho_{\mathrm{L0}}^*U^{*2}}\sin(\tau+G_rR^2) & (0\leqq R\leqq 1),\\ 0 & (1<R),\end{cases}\tag{133}$$

where p_0^* is the amplitude of the source pressure. The wave is only given on the sound source, $0\leqq R\leqq 1$. As shown in Fig. 6, the wave at the sound source ($x^*=0$ mm and $r^*=0$ mm) is amplitude-modulated by the form of the exponential function as in (133). In (133), T_{d} and m are the effective duration and the rise time of pulses, respectively [57,58,60], and set as $T_{\mathrm{d}}=14\pi$ and $m=4$ to radiate approximately 10 pulses.

4.2. Results

In Figs. 7 and 8, the spatial distribution of the first-order dimensional fluctuation of the liquid pressure $p_{\mathrm{L1}}^*=\rho_{\mathrm{L0}}^*U^*\varepsilon p_{\mathrm{L1}}$ at a certain retarded time τ^*, the time development of the liquid pressure p_{L1}^* at a certain point, and the frequency domain of the time development obtained using FFT are shown. The wave distortion of the time development of p_{L1}^* in Figs. 7b and 8b, the generation of higher harmonics in Figs. 7–8c-f are due to the nonlinearity. In Figs. 7a and 8a, the points with the maximum value of p_{L1}^* are approximately $x^*=26$ mm and $x^*=29$ mm, respectively, and are near the sound source of the geometric focal point at $x^*=100$ mm. In Table 2, the parameters and resultant values of the calculation are shown for five different initial void fractions α_0, including the cases shown in Figs. 7 and 8. Because of the assumption (a-5) in Section 2.1, sufficiently small value of initial void fraction is used. In $\alpha_0=0.0001$, the maximum value of p_{L1}^* in the case of water exceeds that of liver tissue. However, in $\alpha_0\geqslant 0.00025$, the maximum values of p_{L1}^* in the cases of liver tissue exceed those of water.

4.3. Effect of dispersion

The dispersion effect is represented in the form of the third derivative with coefficient Π_3 in the resultant KZK equation (102) and obtained by introducing the bubble oscillation [10,25–29,88–95,102,103,113–115]. By the dispersion effect, the propagation speed of waves shifts depending on the frequency of each wave. Hence when the dispersion effect is introduced, higher harmonic components generated by the nonlinear effect will propagate at a speed different from the fundamental frequency component.

Fig. 9 shows the numerical solution that only the dispersion coefficient Π_3 is virtually set as zero to clarify the dispersion effect. In Figs. 7b and 8b with the dispersion effect, some peak points with low values newly appeared among the discontinuous points owing to the dispersion effect. In contrast to Figs. 7b and 8b, the time development of Fig. 9b does not have the new peak points. In addition, tha spatial distribution of Fig. 9a without dispersion effect has the narrower peak region of pressure rise than the Figs. 7a and 8a.

4.4. Generation of higher harmonic

In Fig. 7, the initial void fraction $\alpha_0=0.00025$ and the liquid is water. The frequency domains of Figs. 7c-f show that the fundamental frequency component gradually shift into higher harmonic components. In $x^*=29$ mm and $x^*=32$ mm of Figs. 7e and 7f, the third harmonic components exceed the second harmonic components.

In Fig. 8, the initial void fraction $\alpha_0=0.0005$ and the liquid is liver tissue. The other conditions including the frequency, the pressure amplitude and the radius of sound source, are same as Fig. 7. The

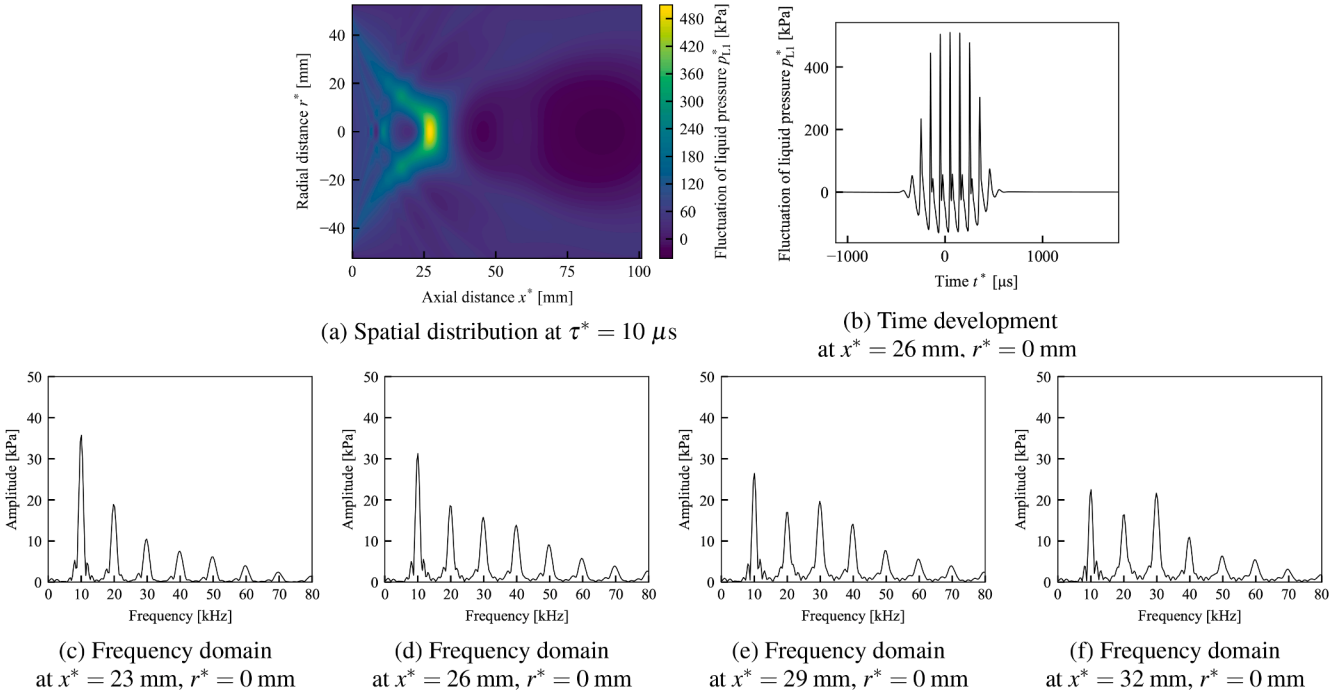

(a) Spatial distribution at $\tau^*=10$ μs

(b) Time development at $x^*=26$ mm, $r^*=0$ mm

(c) Frequency domain at $x^*=23$ mm, $r^*=0$ mm

(d) Frequency domain at $x^*=26$ mm, $r^*=0$ mm

(e) Frequency domain at $x^*=29$ mm, $r^*=0$ mm

(f) Frequency domain at $x^*=32$ mm, $r^*=0$ mm

Fig. 7. The case in which the liquid is water and the initial void fraction is $\alpha_0=0.00025$: (a) spatial distributions of the dimensional fluctuation of the liquid pressure p_{L1}^* at the retarded time $\tau^*=10$ μs; (b) time development at $x^*=26$ mm and $r^*=0$ mm of (a); (c)(d)(e)(f) frequency domains at each point of (a) obtained using the fast Fourier transform. Used parameters: initial bubble radius $R_0^*=100$ μm, frequency of sound source $f^*=10$ kHz, pressure amplitude of sound source $p_0^*=100$ kPa, radius of sound source $a_r^*=50$ mm, and geometric focal length $d_{\mathrm{f}}^*=100$ mm.

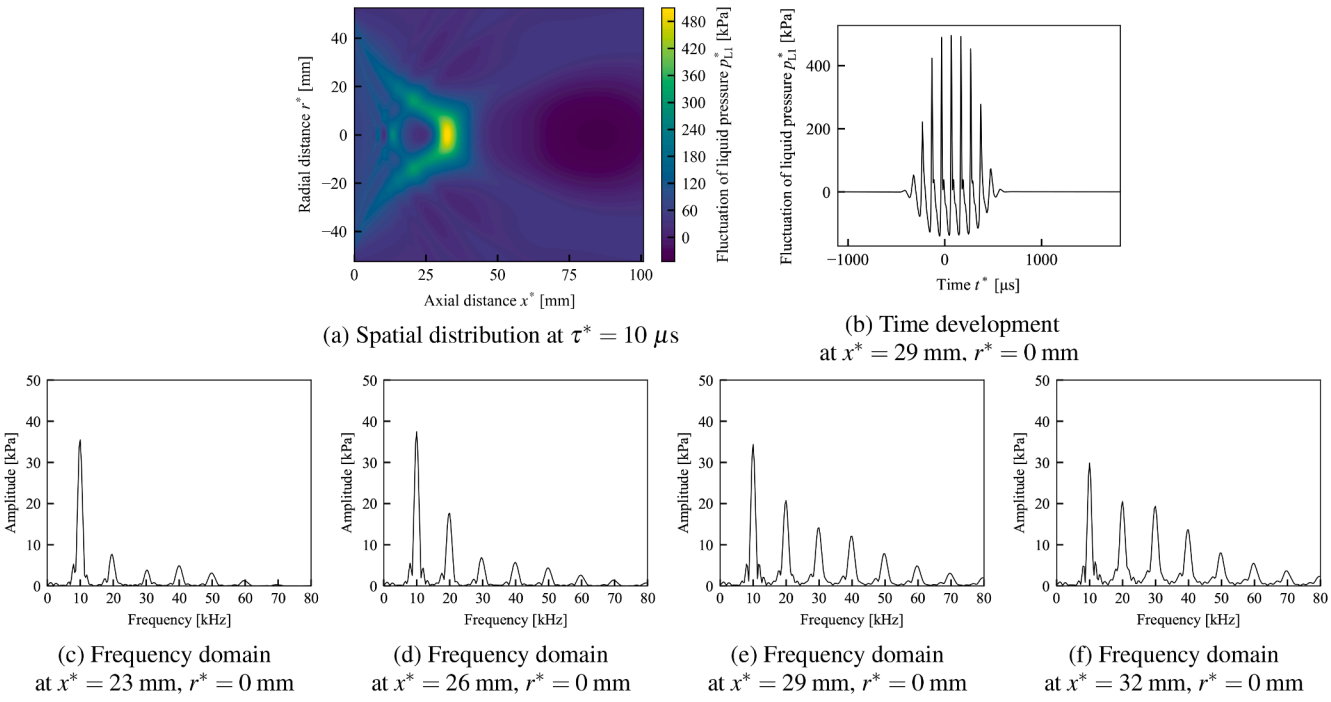

(a) Spatial distribution at $\tau^* = 10\ \mu$s

(b) Time development at $x^* = 29$ mm, $r^* = 0$ mm

(c) Frequency domain at $x^* = 23$ mm, $r^* = 0$ mm

(d) Frequency domain at $x^* = 26$ mm, $r^* = 0$ mm

(e) Frequency domain at $x^* = 29$ mm, $r^* = 0$ mm

(f) Frequency domain at $x^* = 32$ mm, $r^* = 0$ mm

Fig. 8. The case in which the liquid is liver tissue and the initial void fraction is $\alpha_0 = 0.0005$. All the other conditions are the same as in Fig. 7.

Table 2
Parameters and resultant values for five different initial void fractions α_0, including the cases in Figs. 7 and 8. The absolute values of Π_{21} and Π_3 are shown since they are originally negative. Maximum value of p^*_{L1} is at $\tau^* = 10\ \mu$s.

	$\alpha_0 = 0.0001$		$\alpha_0 = 0.00025$		$\alpha_0 = 0.0005$		$\alpha_0 = 0.00075$		$\alpha_0 = 0.001$	
	Water	Liver tissue	Water	Liver tissue	Water	Liver tissue	Water	Liver tissue	Water	Liver tissue
Nonlinear coefficient Π_1 [-]	3.60	3.44	3.60	3.44	3.60	3.44	3.60	3.43	3.60	3.43
Dissipation coefficient $\lvert\Pi_{21}\rvert$ [-]	0.0126	0.0104	0.0200	0.0165	0.0282	0.0233	0.0346	0.0285	0.0399	0.0328
Dissipation coefficient Π_{22} [-]	0.135	0.0883	0.214	0.140	0.303	0.197	0.371	0.241	0.428	0.278
Dispersion coefficient $\lvert\Pi_3\rvert$ [-]	0.241	0.173	0.381	0.274	0.539	0.387	0.660	0.473	0.761	0.546
Phase velocity U^* [m/s]	1197	1336	757	845	536	598	437	488	379	423
Maximum value of p^*_{L1} [kPa]	493	360	506	560	373	505	365	438	347	384

maximum values of pressure fluctuations are 506 kPa and 505 kPa in Figs. 7 and 8, respectively, these values are quite close. As Fig. 7c-f, the frequency domains of Figs. 8c-f show that the fundamental frequency component gradually shift into higher harmonic components, however, third harmonic components do not exceed the second harmonic components in contrast to Fig. 7e and 7f. In addition, Figs. 8c-f retain more fundamental frequency components than Figs. 7c-f. These results imply that the elasticity of the liquid phase suppresses the generation of higher harmonic components and promotes the remnant of the fundamental frequency components; therefore, the elasticity of the liquid phase suppresses shock wave formation in practical applications.

5. Conclusion

Weakly nonlinear propagation of focused ultrasound in viscoelastic liquid containing multiple bubbles was investigated using the volumetric averaged equations of liquid containing multiple bubbles based on the mixture model [96–99]. The viscoelasticity of the entire liquid was introduced to the momentum conservative equation (4) and modeled with the Zener model (16), whereas that of the bubble–liquid interface was considered in the Keller–Miksis equation (17).

As a result of the theoretical analysis based on perturbation expansion with the multiple-scales method [121], the KZK equation (102) describing the weakly nonlinear propagation in viscoelastic liquids containing multiple bubbles was derived. The resultant KZK equation (102) is composed of terms representing nonlinear, dissipation, dispersion, and diffraction effects of ultrasound propagation. As shown in Fig. 3, the liquid elasticity decreases the magnitudes of nonlinear coefficient Π_1, dissipation coefficients Π_{21} and Π_{22}, and dispersion coefficient Π_3, and increases the phase velocity U^* and linear natural frequency of bubble oscillation ω^*_B. As shown in Fig. 4, the comparison among the viscoelastic models; Zener model, Maxwell model, and Kelvin–Voigt model, is conducted. Then, the effects of the rigidity is quite larger than the relaxation time. In addition, a comparison of the liquid viscoelasticity of the entire liquid and bubble–liquid interface was conducted. As shown in Fig. 5, the nonlinear coefficient Π_1 was decreased by both elasticities. However, the magnitudes of the dissipation coefficients Π_{21} and Π_{22}, dispersion coefficient Π_3, phase velocity U^*, and linear natural frequency of the bubble oscillation ω^*_B were strongly affected by the elasticity of the bubble–liquid interface, while the effects of the elasticity of the entire liquid were considerably small.

In Section 4, the numerical solution of the newly obtained KZK equation was shown for different cases of the initial void fraction α_0. The dispersion effect introduced by the bubble oscillation are shown, by virtually setting the dispersion coefficient $\Pi_3 = 0$ of Fig. 9. In addition, a frequency analysis was carried out using FFT and the generation of higher harmonic components was compared for water and liver tissue. As shown in the frequency analysis of Figs. 7–8f, the elasticity of liver tissue suppresses the generation of higher harmonic components and promotes the remnant of the fundamental frequency components

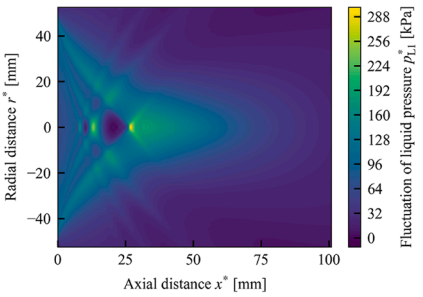

(a) Spatial distribution at $\tau^* = 10\ \mu$s

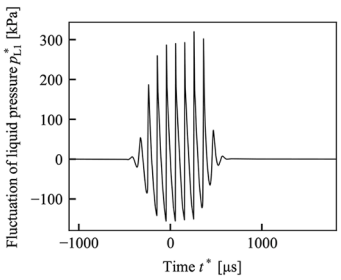

(b) Time development at $x^* = 29$ mm, $r^* = 0$ mm

Fig. 9. The case in which only the dispersion coefficient is set as zero and the other conditions are same as Fig. 8.

compare to the case of water, although the maximum values of p^*_{L1} are quite close. Therefore, this result implies that the elasticity of the liquid phase suppresses shock wave formation in practical applications.

In our future work, theoretical extensions of the KZK equation will be conducted, such as incorporating blood vessels [132–134], phase change [107,109] and heat transfer [110] across bubble–liquid interface, and bubble–bubble interaction [39,44,46,104–106]. Deriving the Westervelt equation as a generalization of the present KZK equation is effective. On the other hand, incorporating the nonlinear dissipation [124–127] will change the resultant equation from KZK equation and Westervelt equation, however will be very important. Ultimately, verifying the present KZK equation by comparison with experimental and direct numerical simulations is necessary.

CRediT authorship contribution statement

Shunsuke Kagami: Software, Validation, Formal analysis, Investigation, Data curation, Writing - original draft, Writing - review & editing, Funding acquisition. **Tetsuya Kanagawa:** Conceptualization, Methodology, Formal analysis, Investigation, Writing - original draft, Writing - review & editing, Supervision, Project administration, Funding acquisition.

Declaration of Competing Interest

The authors declare that they have no known competing financial interests or personal relationships that could have appeared to influence the work reported in this paper.

Acknowledgement

This work was partially carried out with the aid of the Sasakawa Scientific Research Grant from the Japan Science Society, the JSPS KAKENHI (22K03898), the Ono Charitable Trust for Acoustics, the Komiya Research Grant from the Turbomachinery Society of Japan, and the New Energy and Industrial Technology Development Organization (NEDO).

Appendix A. Inhomogeneous terms in (92)–(97)

The inhomogeneous terms $K_i\,(i = 1, \ldots, 6)$ are given as

$$K_1 = 3\frac{\partial \alpha_1 R_1}{\partial t_0} + 3\delta(x_1)\frac{\partial R_1}{\partial t_0} - 6\frac{\partial R_1^2}{\partial t_0} - \frac{\partial \alpha_1}{\partial t_1} + 3\frac{\partial R_1}{\partial t_1} - \frac{\partial \alpha_1 u_{x1}}{\partial x_0} - \delta(x_1)\frac{\partial u_{x1}}{\partial x_0} + 3\frac{\partial R_1 u_{x1}}{\partial x_0} - \frac{\partial u_{x1}}{\partial x_1} - \begin{cases} \Gamma_r\left(\dfrac{u_{r1}}{r_{1/2}} + \dfrac{\partial u_{r1}}{\partial r_{1/2}}\right) & \text{(for 2D case)}, \\ \Gamma_y \dfrac{\partial u_{y1}}{\partial y_{1/2}} + \Gamma_z \dfrac{\partial u_{z1}}{\partial z_{1/2}} & \text{(for 3D case)}, \end{cases} \tag{A.1}$$

$$K_2 = (1-\alpha_0)\frac{\partial \rho_{L1}}{\partial t_0} - \alpha_0 \frac{\partial \alpha_1}{\partial t_1} - \alpha_0 \frac{\partial \alpha_1 u_{x1}}{\partial x_0} - \alpha_0 \delta(x_1)\frac{\partial u_{x1}}{\partial x_0} + (1-\alpha_0)\frac{\partial u_{x1}}{\partial x_1} + \begin{cases} \Gamma_r(1-\alpha_0)\left(\dfrac{u_{r1}}{r_{1/2}} + \dfrac{\partial u_{r1}}{\partial r_{1/2}}\right) & \text{(for 2D case)}, \\ (1-\alpha_0)\left(\Gamma_y \dfrac{\partial u_{y1}}{\partial y_{1/2}} + \Gamma_z \dfrac{\partial u_{z1}}{\partial z_{1/2}}\right) & \text{(for 3D case)}, \end{cases} \tag{A.2}$$

$$K_3 = \alpha_0 \frac{\partial \alpha_1 u_{x1}}{\partial t_0} + \alpha_0 \delta(x_1)\frac{\partial u_{x1}}{\partial t_0} - (1-\alpha_0)\frac{\partial u_{x1}}{\partial t_1} - \frac{\partial p_{L1}}{\partial x_1} + \frac{\partial \tau_{xx1}}{\partial x_1} - (1-\alpha_0)\frac{\partial u_{x1}^2}{\partial x_0} - \frac{2}{3}\mu_L \frac{\partial^2 u_{x1}}{\partial x_0^2} + 2\left(K_{e,L} - \frac{2}{3}G_L\right)\frac{\partial^2 d_{x1}}{\partial x_0 \partial x_1} + \begin{cases} \Gamma_r\left(K_{e,L} - \dfrac{2}{3}G_L\right)\left(\dfrac{1}{r_{1/2}}\dfrac{\partial d_{r1}}{\partial x_0} + \dfrac{\partial d_{r1}}{\partial r_{1/2}\partial x_0}\right) \\ \quad + \Gamma_r\left(\dfrac{\tau_{xr1}}{r_{1/2}} + \dfrac{\partial \tau_{xr1}}{\partial r_{1/2}}\right) \quad \text{(for 2D case)}, \\ \left(K_{e,L} - \dfrac{2}{3}G_L\right)\left(\Gamma_y \dfrac{\partial d_{y1}}{\partial y_{1/2}\partial x_0} + \Gamma_z \dfrac{\partial d_{z1}}{\partial z_{1/2}\partial x_0}\right) \\ \quad + \Gamma_y \dfrac{\partial \tau_{xy1}}{\partial y_{1/2}} + \Gamma_z \dfrac{\partial \tau_{xz1}}{\partial z_{1/2}} \quad \text{(for 3D case)}, \end{cases} \tag{A.3}$$

$$K_4 = -3(\kappa-1)\frac{\partial R_1}{\partial t_1} - \frac{\partial T_{G1}}{\partial t_1} - 3(\kappa-1)(3\kappa-4)R_1\frac{\partial R_1}{\partial t_0} - 3(\kappa-1)\frac{\partial T_{G1}R_1}{\partial t_0} - 3(\kappa-1)u_{x1}\frac{\partial R_1}{\partial x_0} - u_{x1}\frac{\partial T_{G1}}{\partial x_0} - \lambda_G T_{G1}, \tag{A.4}$$

$$K_5 = \Delta^2 \frac{\partial^2 R_1}{\partial t_0^2} - V\Delta \frac{\partial p_{L1}}{\partial t_0} + \left[-4G_L + 3(\kappa - 2)p_{G0} - \frac{\Delta^2}{\Omega^2} \right] R_1^2 + 3p_{G0} R_1 T_{G1} - 4\lambda_{relax,L} G_L \frac{\partial R_1}{\partial t_0} + 4\mu_L \frac{\partial R_1}{\partial t_0}, \tag{A.5}$$

$$K_6 = -\lambda_{relax,L} \frac{\partial \tau_{xx1}}{\partial t_0} + 2\mu_L \frac{\partial u_{x1}}{\partial x_0} + 2G_L \frac{\partial d_{x1}}{\partial x_1}. \tag{A.6}$$

References

[1] I.A.S. Elhelf, H. Albahar, U. Shah, A. Oto, E. Cressman, M. Almekkawy, Diagn. Interv. Imaging 99 (2018) 349–359.
[2] F.J. Fry, N.T. Sanghvi, R.S. Foster, R. Bihrle, C. Hennige, Med. Biol. 21 (1995) 1227–1237.
[3] J. Kennedy, G. Ter Haar, D. Cranston, British, J. Radiol. 76 (2003) 590–609.
[4] S.D. Sokka, T. King, K. Hynynen, Phys. Med. Biol. 48 (2003) 223–241.
[5] Y. Kaneko, T. Maruyama, K. Takegami, T. Watanabe, H. Mitsui, K. Hanajiri, H. Nagawa, Y. Matsumoto, et al., Eur. Radiol. 15 (2005) 1415–1420.
[6] Y. Matsumoto, J.S. Allen, S. Yoshizawa, T. Ikeda, Y. Kaneko, Exp. Therm. Fluid Sci. 29 (2005) 225–265.
[7] F.A. Jolesz, Annu. Rev. Med. 60 (2009) 417–430.
[8] L.C. Moyer, K.F. Timbie, P.S. Sheeran, R.J. Price, G.W. Miller, P.A. Dayton, J. Ther, Ultrasound 3 (2015) 7–16.
[9] N. Chang, S. Lu, D. Qin, T. Xu, M. Han, S. Wang, M. Wan, Ultrason. Sonochem. 45 (2018) 57–64.
[10] S. Kagami, T. Kanagawa, Ultrason. Sonochem. 88 (2022), 105911.
[11] A.D. Maxwell, T.Y. Wang, C.A. Cain, J.B. Fowlkes, O.A. Sapozhnikov, M.R. Bailey, Z. Xu, J. Acoust. Soc. Am. 130 (2011) 1888–1898.
[12] W.W. Roberts, Curr. Opin. Urol. 24 (2014) 104–110.
[13] E. Vlaisavljevich, K.W. Lin, A. Maxwell, et al., Ultrasound Med. Biol. 41 (2014) 1651–1667.
[14] K.B. Bader, K.J. Haworth, Shekhar, et al., Phys. Med. Biol. 61 (2016) 5253–5274.
[15] J.R. Sukovich, C.A. Cain, A.S. Pandey, et al., J. Neurosurg. 131 (2018) 1–8.
[16] K.B. Bader, E. Vlaisavljevich, A.D. Maxwell, Ultrasound Med. Biol. 45 (2019) 1056–1080.
[17] Z. Xu, T.L. Hall, E. Vlaisavljevich, F.T. Lee, Int. J. Hyperth. 38 (2021) 561–575.
[18] C. Edsall, Z.M. Khan, L. Mancia, S. Hall, W. Mustafa, E. Johnsen, A.L. Klibanov, Y. Y. Durmaz, E. Vlaisavljevich, Ultrasound Med. Biol. 47 (2021) 620–639.
[19] L. Mancia, E. Vlaisavljevich, N. Yousefi, et al., Phys. Med. Biol. 64 (2019), 225001.
[20] X. Zhen, H.L. Timothy, E. Vlaisavljevich, T.F. Lee Jr, Int. J. Hyperth. 38 (2021) 561–575.
[21] N.A. Lapin, K. Gill, B.R. Shah, R. Chopra, Sci. Rep. Uk 10 (2020) 16546.
[22] C.H. Wang, Y.F. Huang, C.K. Yeh, Langmuir 27 (2011) 6971–6976.
[23] W.K. Chong, V. Papadopoulou, P.A. Dayton, Abdom. Radiol 43 (2018) 762–772.
[24] J. Zhu, N. Tagawa, Jpn. J. Appl. Phys. 58 (2019) SGGE03.
[25] Y. Kikuchi, T. Kanagawa, Jpn. J. Appl. Phys. 60 (2021) SDDD14.
[26] Y. Kikuchi, T. Kanagawa, T. Ayukai, Chem. Eng. Sci. 269 (2023), 117541.
[27] T. Kanagawa, M. Honda, Y. Kikuchi, Phys. Fluids. 35 (2023), 023303.
[28] R. Kawahata, T. Kanagawa, G. Chabouh, Phys. Fluids. 35, in press (2023). https://dx.doi.org/10.1063/5.0141983.
[29] N.Q. Nguyen, T. Kanagawa, Nonlinear Dyn. 111 (2023) 10859–10877.
[30] D.A. Gubaidullin, Y.V. Fedorov, J. Hydrodyn. 33 (2021) 55–62.
[31] D.A. Gubaidullin, D.D. Gubaidullina, Y.V. Fedorov, Mathematics 11 (2023) 1083.
[32] J.M. Carcione, F. Poletto, D. Gei, J. Comput. Phys. 196 (2004) 1282–1297.
[33] B.E. Treeby, J. Jaros, D. Rohrbach, B.T. Cox, 2014 IEEE International Ultrasonics Symposium 146–149 (2014). https://doi.org/10.1109/ULTSYM.2014.0037.
[34] X. Yang, C.C. Church, J. Acoust. Soc. Am. 118 (2005) 3595–3606.
[35] R. Gaudron, M. Warnez, E. Johnsen, J. Fluid Mech. 766 (2015) 54–75.
[36] L. Mancia, E. Vlaisavljevich, Z. Xu, E. Johnsen, Ultrasound Med. Biol. 43 (2017) 1421–1440.
[37] K. Murakami, R. Gaudron, E. Johnsen, Ultrason. Sonochem. 67 (2020), 105170.
[38] J. Estrada, C. Barajas, D. Henann, E. Johnsen, J. Mech. Phys. Solids 112 (2018) 291–317.
[39] D. Qin, Q. Zou, S. Lei, W. Wang, Z. Li, Ultrason. Sonochem. 78 (2021), 105712.
[40] A.K. Abu-Nab, K.G. Mohamed, A.F. Abu-Bakr, Arch, Appl, Mech, 2022.
[41] C. Hua, E. Johnsen, Phys. Fluids 25 (2013), 083101.
[42] M.T. Warnez, E. Johnsen, Phys. Fluids 27 (2015), 063103.
[43] M. Rodriguez, E. Johnsen, J. Comput. Phys. 379 (2019) 70–90.
[44] D. Qin, Q. Zou, S. Lei, W. Wang, Z. Li, Micromachines 12 (2021) 1125.
[45] E. Zilonova, M. Solovchuk, T. Sheu, Ultrason. Sonochem. 40 (2018) 900.
[46] E. Zilonova, M. Solovchuk, T. Sheu, Phys. Rev. E 99 (2019), 023109.
[47] T. Filonets, M. Solovchuk, Ultrason. Sonochem. 88 (2022), 106056.
[48] H.S. Fogler, J.D. Goddard, Phys. Fluids 13 (1970) 1135.
[49] J. Allen, R. Roy, J. Acoust. Soc. Am. 107 (2000) 3167.
[50] M. Ichihara, H. Ohkunitani, Y. Ida, M. Kameda, Dynamics of bubble oscillation and wave propagation in viscoelasti liquids, J. Volcanol Geotherm. Res. 129 (2004) 37.
[51] E. Brujan, Cavitation in Non-Newtonian Fluids, Springer, Heidelberg, 2011.
[52] K.B. Keller, M. Miksis, J. Acoust. Soc. Am. 68 (1980) 628–633.
[53] F.R. Gilmore, Hydrodynamics laboratory, California Institute of Technology, Pasadena, California, 1952.
[54] P. Westervelt, J. Acoust. Soc. Am. 35 (1965) 535–537.
[55] E.A. Zabolotskaya, R.V. Khokhlov, Sov. Phys. Acoust. 15 (1969) 35–40.
[56] V.P. Kuznetsov, Sov. Phys. Acoust. 16 (1971) 467–470.
[57] Y.S. Lee, Ph. D. dissertation, The University of Texas at Austin (1993).
[58] Y.S. Lee, M.F. Hamilton, J. Acoust. Soc. Am. 97 (1995) 906–917.
[59] R.O. Cleveland, M.F. Hamilton, D.T. Blackstock, J. Acoust. Soc. Am. 99 (1996) 3312–3318.
[60] M.A. Averkiou, M.F. Hamilton, J. Acoust. Soc. Am. 102 (1997) 2539–2548.
[61] M.A. Averkiou, R.O. Cleveland, J. Acoust. Soc. Am. 106 (1999) 101–112.
[62] R. Williams, E. Cherin, T.Y.J. Lam, J. Tavakkoli, R.J. Zemp, F.S. Foster, Phys. Med. Biol. 51 (2006) 5809–5824.
[63] P. Hariharan, M.R. Myers, R.A. Robinson, S.H. Maruvada, J. Sliwa, R.K. Banerjee, J. Acoust. Soc. Am. 123 (2008) 1706–1719.
[64] A. Bhargava, K. Peng, J. Stieg, R. Mirzaeifar, S. Shahab, RSC Adv. 7 (2017) 45452.
[65] S.L. Liu, Y.Y. Yang, C.H. Li, X.S. Guo, J. Tu, D. Zhang, Applied Sciences, Basel 8 (2018).
[66] S. Haddadi, M.T. Ahmadian, J. Ultrasound Med. 37 (2018) 1481–1491.
[67] C. Vanhille, K. Hynynen, Acoustics 1 (2019) 825–836.
[68] M. Bakhtiari-Nejad, S. Shahab, Acoustics 1 (2019) 14–34.
[69] E.A. Filonenko, V.A. Khokhlova, Acoust. Phys. 47 (2001) 541–549.
[70] V.A. Khokhlova, R. Souchon, J. Tavakkoli, O.A. Sapozhnikov, D. Cathignol, J. Acoust. Soc. Am. 110 (2001) 95–108.
[71] X. Yang, R.O. Cleveland, J. Acoust. Soc. Am. 117 (2005) 113–123.
[72] T. Varslot, G. Taraldsen, IEEE Trans. Ultrason. Ferroelectr. Freq. Control 52 (2005) 1473–1482.
[73] V.A. Khokhlova, A.E. Ponomarev, M.A. Averkiou, L.A. Crum, Acoust. Phys. 52 (2006) 481–489.
[74] V.A. Khokhlova, M.R. Bailey, J.A. Reed, B.W. Cunitz, P.J. Kaczkowski, L.A. Crum, J. Acoust. Soc. Am. 119 (2006) 1834–1848.
[75] X.Z. Liu, J.L. Li, X.F. Gong, D. Zhang, Ultrasonics 44 (2006) e27–e30.
[76] J.L. Li, X.Z. Liu, D. Zhang, X.F. Gong, Ultrasound Med. Biol. 33 (2007) 1413–1420.
[77] Y. Jing, R.O. Cleveland, J. Acoust. Soc. Am. 122 (2007) 1352–1364.
[78] A. Rozanova-Pierrat, Commun. Math. Sci. 7 (2009) 679–718.
[79] T. Khokhlova, M. Canney, D. Lee, K. Marro, L. Crum, V. Khokhlova, M. Bailey, J. Acoust. Soc. Am. 125 (2009) 2420–2431.
[80] X.Z. Liu, C. Yin, X.F. Gong, W.W. Cao, Ultrasound Med. Biol. 36 (2010) 1704–1712.
[81] O.A. Kaya, D. Kaleci, A. Şahin, Acoust. Phys. 57 (2011) 127–135.
[82] E.V. Dontsov, B.B. Guzina, Wave Motion 50 (2013) 763–775.
[83] M.H. Hasani, S. Gharibzadeh, Y. Farjami, J. Tavakkoli, J. Acoust. Soc. Am. 134 (2013) 1775–1790.
[84] J. Gu, Y. Jing, IEEE Trans. Ultrason. Ferroelectr. Freq. Control 62 (2015) 1979–1993.
[85] B. Maraghechi, M.H. Hasani, M.C. Kolios, J. Tavakkoli, J. Acoust. Soc. Am. 139 (2016) 2475–2481.
[86] S. Qiao, E. Jackson, C.C. Coussios, R.O. Cleveland, J. Acoust. Soc. Am. 140 (2016) 2039–2046.
[87] H. Li, J. Ma, J. Zhu, B. Chen, Shock Vib. (2019).
[88] T. Kanagawa, T. Yano, M. Watanabe, S. Fujikawa, J. Fluid Sci. Technol. 6 (2011) 279–290.
[89] T. Yano, T. Kanagawa, M. Watanabe, S. Fujikawa, in Shock Wave Science and Technology Reference Library, Springer, 2013.
[90] T. Kanagawa, J. Acoust. Soc. Am. 137 (2015) 2642–2654.
[91] T. Hasegawa, T. Kanagawa, Phys. Fluids 35 (2023) 043309. https://doi.org/10.1063/5.0131091.
[92] T. Kanagawa, T. Yano, M. Watanabe, S. Fujikawa, J. Fluid Sci. Technol. 5 (2010) 351–369.
[93] S. Kagami, T. Kanagawa, Jpn. J. Multiphase Flow 35 (2021) 346–355.
[94] T. Kamei, T. Kanagawa, T. Ayukai, Phys. Fluids 33 (2021), 053302.
[95] T. Kanagawa, T. Kamei, Phys. Fluids 33 (2021), 063319.
[96] M. Ishii, ANL Report No. ANL-77-47 (1977). https://doi.org/10.2172/6871478.
[97] I. Kataoka, Jpn. J. Multiphase Flow 5 (1991) 3–21.
[98] I. Akhatov, U. Parlitz, W. Lauterborn, Phys. Rev. E 54 (1996) 4990–5003.
[99] R. Egashira, T. Yano, S. Fujikawa, Fluid Dyn. Res. 34 (2004) 317–334.
[100] T. Ayukai, T. Kanagawa, Int. J. Multiph. Flow 165 (2023), 104456.
[101] G. Zhou, A. Prosperetti, J. Fluid Mech. 901 (2020) R3.
[102] T. Yatabe, T. Kanagawa, T. Ayukai, Phys. Fluids 33 (2021), 033315.
[103] S. Arai, T. Kanagawa, T. Ayukai, J. Phys. Soc. Jpn. 91 (2022), 043401.
[104] D. Fuster, J.M. Conoir, T. Colonius, Phys. Rev. E 90 (2014), 063010.
[105] M. Guédra, C. Cornu, C. Inserra, Ultrason. sonochem. 38 (2017) 168–173.
[106] A.J. Sojahrood, R. Earl, H. Haghi, Q. Li, T.M. Porter, M.C. Kolios, R. Karshafian, Nonlinear Dyn. 103 (2021) 429–466.
[107] D. Fuster, F. Montel, J. Fluid Mech. 779 (2015) 598–621.
[108] A. Prosperetti, Interface focus 5 (2015) 20150024.

[109] K. Kerboua, S. Merouani, O. Hamdaoui, A. Alghyamah, M.H. Islam, H.E. Hansen, B.G. Pollet, Ultrason. Sonochem. 72 (2020), 105422.
[110] Y. Zhang, S. Li, Int. Commun. Heat Mass Transf. 53 (2014) 43–49.
[111] K.W. Commander, A. Prosperetti, J. Acoust. Soc. Am. 85 (1989) 732–746.
[112] E.M.A. Frederix, T.L.W. Cox, J.G.M. Kuerten, E.M.J. Komen, Chem. Eng. Sci. 201 (2019) 237–246.
[113] T. Kawame, T. Kanagawa, Int. J. Multiph. Flow 164 (2023), 104369.
[114] T. Kanagawa, T. Ayukai, T. Kawame, R. Ishitsuka, Int. J. Multiph. Flow 142 (2021), 163622.
[115] T. Kanagawa, R. Ishitsuka, S. Arai, T. Ayukai, Phys. Fluids 34 (2022), 103320 .
[116] A. Prosperetti, J. Fluid Mech. 222 (1991) 587–616.
[117] M. Shimada, Y. Matsumoto, T. Kobayashi, Trans. JSME, Ser. B 65, 1934–1940 (1999). https://doi.org/10.1299/kikaib.65.1934.
[118] B. Lertnuwat, K. Sugiyama, Y. Matsumoto, in Proceedings of 4th International Symposium on Cavitation, B6.002 (2001).
[119] A. Preston, T. Colonius, C.E. Brennen, in Proceedings of ASME FEDSM'02, FEDSM2002-31026(CD-ROM) (2002).
[120] K. Sugiyama, S. Takagi, Y. Matsumoto, Trans. JSME, Ser. B 71, 1011–1019 (2005). https://doi.org/10.1299/kikaib.71.1011.
[121] A. Jeffrey, T. Kawahara, Asymptotic Methods in nonlinear wave theory, Pitman, London, 1982.
[122] T. Segers, N. de Jong, M. Versluis, J. Acoust. Soc. Am. 140 (2016) 2506–2517.
[123] A.J. Sojahrood, Q. Li, H. Haghi, R. Karshafian, T.M. Porter, M.C. Kolios, arXiv preprint arXiv:1811.07788 (2018). https://doi.org/10.48550/arXiv.1811.07788.
[124] O. Louisnard, Ultrason. Sonochem. 19 (2011) 56–65.
[125] A.J. Sojahrood, H. Haghi, Q. Li, T.M. Porter, R. Karshafian, M.C. Kolios, Ultrason. Sonochem. 66 (2020), 105070.
[126] A.J. Sojahrood, H. Haghi, R. Karshafian, M.C. Kolios, Ultrason. Sonochem. 66 (2020), 105089.
[127] A.J. Sojahrood, H. Haghi, R. Karshafian, M.C. Kolios, Phys. Fluids 33 (2021), 016105.
[128] C. Chui, E. Kobayashi, X. Chen, T. Hisada, I. Sakuma, Med. Biol. Eng. Comput. 42 (2004) 787–798.
[129] Y. Zhang, S. Li, Ultrason. Sonochem. 35 (2017) 431–439.
[130] M. Guédra, C. Inserra, G. Gilles, Ultrason. Sonochem. 83 (2017) 298–305.
[131] H. Sasaki, J. Yasuda, T. Takagi, T. Miyashita, K. Goto, S. Yoshizawa, S. Umemura, Jpn. J. Appl. Phys. 53 (2014) 07KF11.
[132] E. Sassaroli, K. Hynynen, Phys. Med. Biol. 50 (2005) 5293–5305.
[133] N. Hosseinkhah, H. Chen, T.J. Matula, P.N. Burns, K. Hynynen, J. Acoust. Soc. Am. 134 (2013) 1875–1885.
[134] N. Hosseinkhah, D.E. Goertz, K. Hynynen, IEEE. Trans, Biomed. Eng. 62 (2014) 1293–1304.